# Multi Parameter Fluorescence Spectroscopy -

# Setup, Assembly and Applications

Diplomarbeit aus dem Fachgebiet

Physikalische Chemie

von

cand. chem. **Nikolaus Naredi-Rainer**

geboren am 14. Januar 1984

in Graz

für die Diplomhauptprüfung in der Chemie an der

**Ludwig-Maximilians-Universität**

Datum der mündlichen Prüfung: 17. Juli 2008

Beginn der Diplomarbeit: 17. September 2008

Diplomarbeit beim Prüfungsausschuß eingereicht am: 17. März 2009

# Erklärung

Ich versichere hiermit, dass ich die vorgelegte Diplomarbeit am Department Chemie, Physikalische Chemie der Ludwig-Maximilians Universität, München, unter der Anregung von Prof. Don C. Lamb, PhD, selbständig durchgeführt und keine anderen als die angegebenen Hilfsmittel und Quellen benutzt habe.

München, den 17. März 2009

| | |
|---|---|
| Erstgutachter: | Prof. Don C. Lamb, PhD |
| Zweitgutachter: | Prof. Dr. Jens Michaelis |

Hab Sonne im Herzen und Pizza im Bauch,

dann bist Du glücklich und satt bist Du auch!

# Acknowledgements

Mein herzliches vergelts Gott gilt all jenen die ein Stück dieses Weges mit mir gegangen sind!

ENTRANCE AND EXIT

# Abstract

Confocal fluorescence spectroscopy enables investigation of structure and dynamics of biomolecules. The development of photostable fluorophores and highly sensitive detectors over the last decades made single-molecules accessible by confocal spectroscopy. The extraction of the maximum possible information from every arriving photon allows an increasing number of applications. In the present work, a new Multi Parameter Fluorescence Setup (MPF) was established, which provides several types of information: the arrival time, wavelength and polarization of the photon, the source it is derived from - as soon as more than one laser is used to excite the sample - and the point of time the photon was emitted relative to the excitation. Hence, this last information allows to infer on the lifetime of the dye.

The setup was fully characterized and the adaptability, ranging from measuring FRET efficiencies and fundamental anisotropies to the calculation of diffusion processes with the help of FCS, was shown.

The MPF setup was used to reveal the ATP dependency of the Heat Shock Protein 90 (HSP90). Up to now, it is not clear how the hydrolysis of ATP influences the opening and closing of this homo-dimer. In this study, several mutants of HSP90 were measured and their FRET efficiencies calculated. Thus, the prevailing state of knowledge could be partly confirmed and extended.

In order to gain a detailed insight into the polymerization of actin, we proved that with the MPF setup it is possible to follow the polymerization of actin over 48 hours. Several parameters that influence the critical concentration and the velocity of the polymerization were varied. In preliminary results we could show the correlation of monomer concentration to overall count rate and the influence of phalloidin on the diffusion behaviour of actin monomers.

# Contents

**CHAPTER 1: INTRODUCTION ........ 1**

AIMS OF THIS WORK ........ 3

**CHAPTER 2: THE FUNDAMENTALS OF FLUORESCENCE SPECTROSCOPY ........ 5**

2.1 JABLONSKI DIAGRAM ........ 5

*2.1.1 Absorption and Emission-Spectra ........ 6*

*2.1.2 Fluorescence Lifetime ........ 7*

*2.1.3 Quenching of Fluorescence ........ 8*

*2.1.4 Quantum Efficiency ........ 8*

2.2 FLUORESCENCE RESONANCE ENERGY TRANSFER ........ 10

2.3 FLUORESCENCE ANISOTROPY ........ 13

2.4 CONFOCAL MICROSCOPY ........ 14

**CHAPTER 3: THEORY OF ANALYSIS METHODS ........ 15**

3.1 PULSED INTERLEAVED EXCITATION ........ 15

3.2 FLUORESCENCE CORRELATION SPECTROSCOPY ........ 18

*3.2.1 Autocorrelation ........ 18*

*3.2.2 Cross-Correlation ........ 21*

3.3 BURST ANALYSIS ........ 24

**CHAPTER 4: RESULTS AND DISCUSSION ........ 28**

4.1 MUTIPARAMETER SETUP ........ 28

*4.1.1 Configuration of the MPF-Setup ........ 28*

*4.1.2 Characterization of the Setup ........ 32*

*4.1.3 Discussion of the MPF Setup ........ 38*

4.2 CONFORMATIONAL CHANGES IN HEAT SHOCK PROTEIN 90 ........ 41

*4.2.1 Biochemical Introduction to Heat Shock Protein 90 ........ 41*

*4.2.2 Conformational Changes in HSP 90 Mutants ........ 44*

*4.2.3 Results of various HSP90 mutants ........ 45*

*4.2.4 Discussion of HSP90 Data ........ 48*

4.3 DETAILED INSIGHT IN THE POLYMERIZATION OF ACTIN ........ 50

*4.3.1 Biochemical Introduction to Actin ........ 50*

*4.3.2 Results of the Polymerization of Actin ........ 52*

*4.3.3 Discussion of the Polymerization of Actin ........ 54*

**CHAPTER 5: SUMMARY AND OUTLOOK ........ 55**

5.1 MPF-SETUP ........ 55

5.2 HEAT SHOCK PROTEIN 90 .......... 56
5.3 ACTIN .......... 57

**ABBREVIATIONS .......... 59**

**REFERENCES .......... 60**

# Chapter 1: Introduction

The sophisticated dynamic processes in living organisms can only take place by cooperation of a nearly countless number of complex biomolecules. Often, these biomolecules operate far from thermal equilibrium with the help of energy that living systems gain from food and sunlight.

Biomolecules consist mostly of carbon, nitrogen, oxygen and hydrogen. These atoms form the monomeric building blocks like amino acids, nucleotides, monosaccharides or fatty acids, which in turn are used to construct macromolecules like proteins, nucleic acids, polysaccharides or lipids. Not only the primary and secondary structure, i.e. the sequence of the monomers and intramolecular hydrogen bonds play an important role, but also the tertiary structure is essential for the functionality of biomolecules. As single molecules, they obey physical and chemical laws, but when interacting with other specific molecules, they show exceptional behaviour that a random array of biomolecules would never feature. Entire interaction pathways within a cell are often too complex to explore at once, so it is beneficial to study the function of the single components and subsequently learn about their role in the whole procedure.

The correlation of the behaviour of a single molecule to that of an ensemble of molecules is given by statistical thermodynamics - particularly by the ergodic theorem. This proposition indicates that the temporal average of a certain property of a single molecule is equal to the ensemble average of the associated property at a single time-point. This allows a comprehensive description and utilization of chemical reactions. The outcome and accuracy can be seen in the achievements of modern chemistry, biochemistry and molecular biology.

The limitations of this fundamental chemical understanding occur when one turns to more sophisticated schemes - especially the already mentioned biochemical systems. Characterizations of molecular processes are handicapped with increasing degrees of freedom. The analysis of bio-macromolecules, for example, can appear as a nearly irresolvable problem for ensemble measurements, because differences between distinct active species are lost in the average of the bulk experiment.

In contrast, single-molecule methods measure the statistical distribution of molecular properties, which can be of statically or dynamically heterogeneity. An example is an enzyme, which can engage different conformations. Furthermore, in a single-molecule experiment, it is possible to observe dynamical changes directly such as conformational changes or the kinetics of basic reaction steps.

Surprisingly, the first work on single-molecule detection via fluorescence didn't attract much interest (1). Still, up to now, there are only a few methods, which are capable of making a single-molecule visible in its natural environment:

To make intra- and intermolecular interactions and dynamics observable, force microscopy, like *optical* (2) or *magnetic* (3) *tweezers* and *atomic force microscopy* (AFM) (4) is often used to measure forces of interactions down to piconewtons. Apart from force microscopy, fluorescence spectroscopy and microscopy methods such as *wide-field microscopy* (5), *total internal reflection microscopy* (6) and *confocal fluorescence microscopy* (7) have gained much influence over the last decades.

Since the first successful experiments on single-molecule detection by optical methods (8), experimental and analytical techniques have significantly improved and, at present, allow not only fundamental studies of dynamic and conformational properties of single biomolecules (9), but also offer the potential to establish molecular profiles of species present at very low concentrations or quantities (10). For this purpose, high sensitivity and selectivity are required. This is realized by exciting just the relevant molecules, which are either autofluorescent molecules such as chlorophyll or tryptophan, or with biomolecules orderly labelled with a fluorescent dye. The technique of confocal microscopy, which is used in this work, has not only the advantage of making single molecules visible, but also detects light only from a very small volume of the sample, allowing a much higher resolution in image spectroscopy, for example.

Considering molecular systems, changes in fluorescence parameters of a single, coupled fluorophore sometimes do not provide enough information for a unique molecular identification or for more detailed investigations of molecular interactions. Further information can be obtained on the single molecule level by having more than one fluorophore per particle involved, thereby creating the possibility to determine stoichiometries and detect interactions of individual particles from photon densities and coincidences. Moreover, the use of two fluorescing reporters also makes it possible to determine structural features of particles via fluorescence resonance energy transfer (FRET), quantitatively described by Förster (11). In FRET, energy is transferred from a donor to an acceptor dye. The efficiency of this process depends on the distance between the two dyes and therefore FRET provides a sensitive tool to yield inter- and intramolecular distance information. FRET measurements work very precisely in a distance range from 20 - 100Å. Hence, it is called a molecular ruler (12). In practice, FRET has frequently and successfully been used to investigate biomolecular structures and to follow dynamic processes, including motor proteins at work (13), protein and nucleic acid structure fluctuations (14), and molecular assembly and disassembly (15).

Movements of fluorescently labelled molecules can be studied via their resulting signal fluctuations in confocal measurements due to the very small detection volume. With Fluorescence Correlation Spectroscopy (FCS), it is not only possible to determine the average number of particles that are located inside the confocal volume, but also the time they need to diffuse through the volume (16). This technique can be customized to one's needs by either using two-focus-FCS (17), which allows a much more precise determination of the diffusion constant of any fluorescent molecule or by using two-photon-FCS (18), that excites just the sample within the confocal spot. Furthermore, two-colour Fluorescence-Cross-Correlation-Spectroscopy (FCCS) can investigate reactions and interactions of two different labelled molecules (19). Last, but not least, nearly every fluorescence technique can be enhanced by the use of Pulsed Interleaved Excitation (PIE) (20). This approach allows the assignment of every fluorescence-photon to the source from which it was emitted.

Fluorescence microscopy is a sensitive, specific and non-invasive method that allows one also to assess biochemical information in living cells (21). The overall ambition of our approach to fluorescence microscopy is to get out the maximum amount of information of every arriving photon. Figure 1 shows the several parameters for incoming photons: the arrival time, wavelength, the polarization of the photon, the excitation source (when more than one laser excites the sample and the point of time the photon was emitted relative to the excitation is known). This last piece of information also allows determination of the lifetime of the dye.

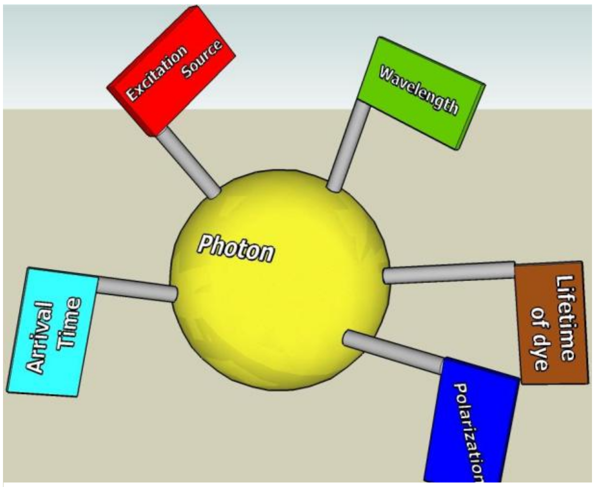

Figure 1: Information inculded in every photon

## Aims Of This Work

This work presents the assembly of a Multi-Parameter Fluorescence (MPF) setup with the ability to make the information included in every photon visible. After a short introduction to the theory of fluorescence (chapter 2) and the analysis methods (chapter 3), the assembly and the characterization of the setup is presented in chapter 4.1. The conformational changes of several mutants of Heat Shock Protein 90 during ATP binding and hydrolyses are examined in chapter 4.2. In chapter 4.3 the potential of the setup is used to investigate the processes that occur during the polymerization of actin. A summary and outlook of the results of this work is presented in chapter 5.

# Chapter 2: The fundamentals of fluorescence spectroscopy

Fluorescence is an optical phenomenon in which the molecular absorption of a photon triggers the emission of a photon with a longer (less energetic) wavelength. The energy difference between the absorbed and emitted photons is converted into molecular rotations, vibrations or heat. The term 'fluorescence' was coined by George Gabriel Stokes (G. Stokes 1852); the name was given as a description of the essence of the mineral fluorite, composed of calcium fluoride, which gave a visible emission when illuminated with "invisible radiation" (UV radiation). The more general term photoluminescence describes the process in which a substance absorbs photons (electromagnetic radiation) and then re-radiates photons. Quantum mechanically, this can be described as an excitation to a higher energy state and then a return to a lower energy state accompanied by the emission of a photon. Photoluminescence can be divided into fluorescence, delayed fluorescence and phosphorescence. The relation between these three forms is shown in a Jablonski diagram (Figure 2).

## 2.1 Jablonski diagram

Fluorescence activity can be schematically illustrated with the classical Jablonski diagram. Prior to excitation, the electronic configuration of the molecule is described as being in the electrical ground state ($S_0$).

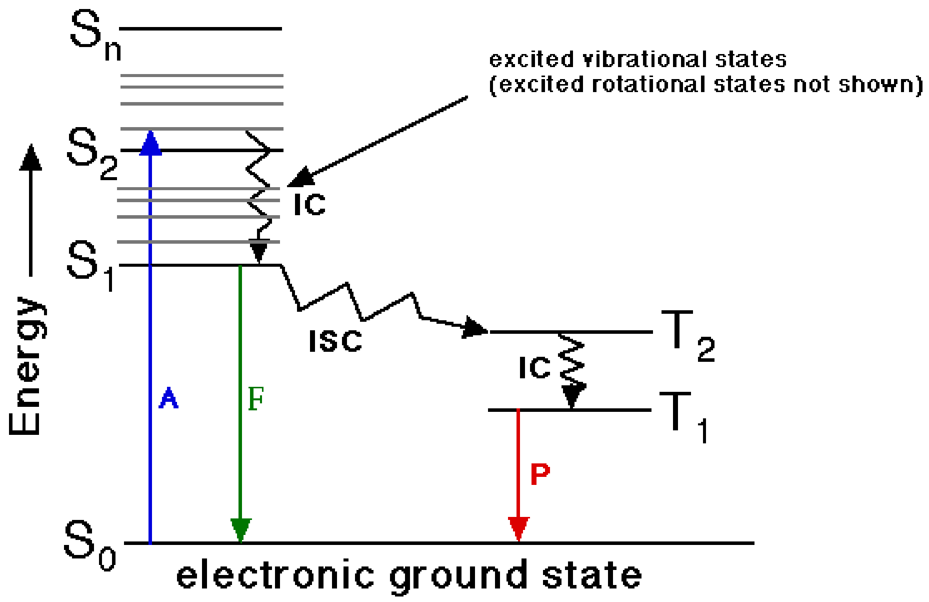

Figure 2: Jablonski diagram showing processes involved in fluorescence: A=photon absorption, F=fluorescence, P=phosphorescence, S=singlet state, T=triplet state, IC=internal conversion, ISC=intersystem crossing

Upon absorbing a photon of light, electrons are excited to a higher energy state ($S_N$), a process that takes only a few femto-seconds. Electronic transitions are essentially instantaneous compared with the time scale of nuclear motions (Born-Oppenheimer approximation). When the electron moves to a new vibrational level during the electronic transition, this new vibrational level must be instantaneously compatible with the nuclear positions and momenta of the vibrational level of the molecule in the originating electronic state (see Figure 3a) ).

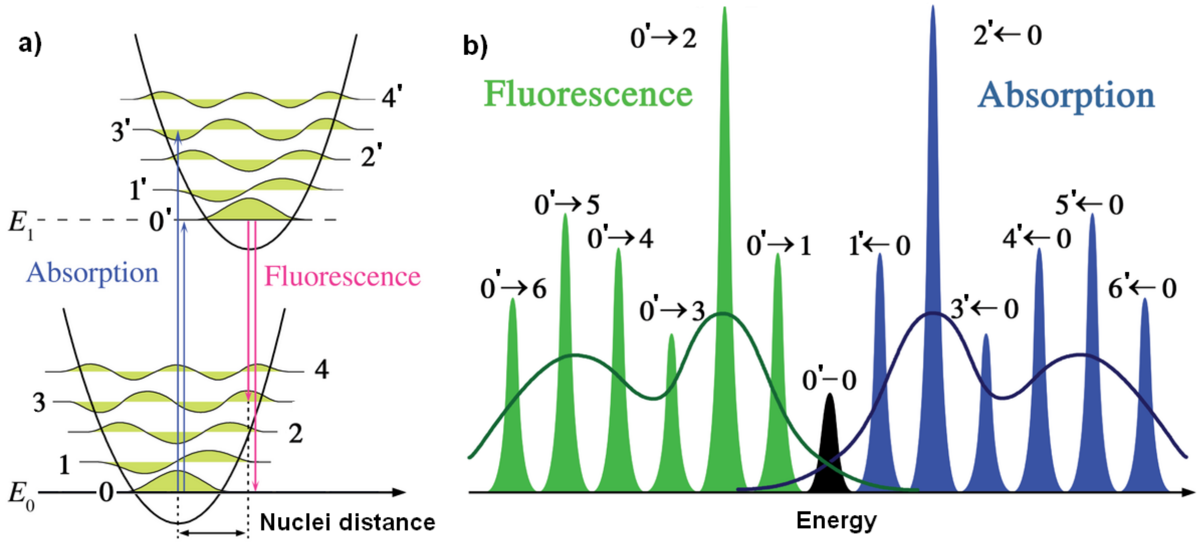

Figure 3: Visualization of a) the Franck-Condon-Principle b) the Stokes Shift

Hence, for excitation or also for deexcitation the Franck-Condon principle states, that after excitation the molecule is not in the vibrational ground state of the $S_N$-state, but in a higher vibrational level. Vibrational relaxation allows the electron to fall back into the ground state of $S_1$. By spontaneous emission of a photon, the molecule is able to return to the ground state. This event is called fluorescence. Two other processes compete with fluorescence: internal conversion (IC), a non-radiative decay where the energy is transferred to the environment or intersystem crossing (ISC). Here, an electron undergoes a transition from a singlet to a triplet state. These transitions, although "forbidden", will still occur if the spin-orbit interaction is strong enough. However, they are kinetically unfavoured and thus process of a decay to the ground state occurs at significantly slower time scales.

There are several important consequences, that arise from the Jablonski diagram. They will be briefly explained in the next sectors.

### 2.1.1 Absorption and Emission-Spectra

A fluorescent dye is usually characterized by its absorption, excitation and emission spectra. The absorption spectrum is the absorbance as a function of wavelength. An emission spectrum shows the intensity of the fluorescence as a function of the wavelength with constant excitation. The emission of a photon usually proceeds from the vibrational ground state of $S_1$, as shown in Figure 3a). As a consequence of this and because the vibrational levels of every $S_N$-state are approximately equidistant, the absorption and emission spectra are mirrored and the emission is shifted to lower energies (Figure 3b). This shift is called the Stokes-Shift.

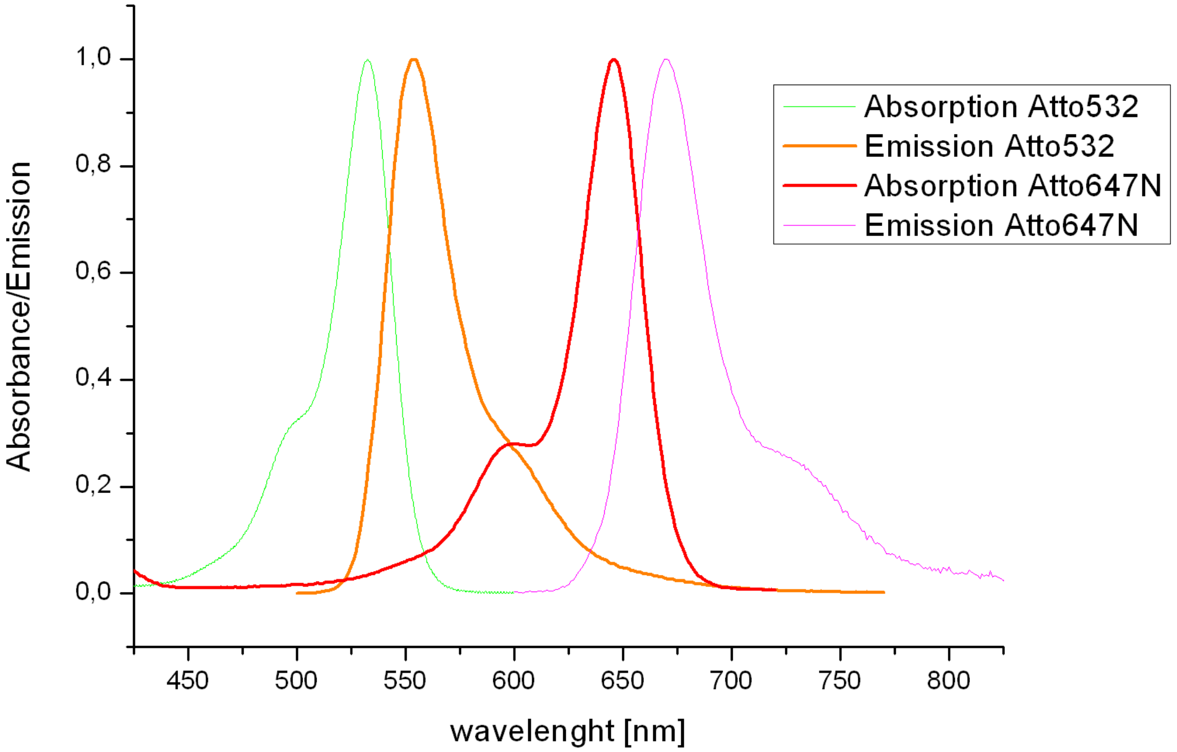

Figure 4: Absorption and emission spectra of Atto532 and Atto647N

The absorption and emission spectra of the two dyes Atto532 and Atto647N are shown in Figure 4.

## 2.1.2 Fluorescence Lifetime

Not only different spectra distinguish a fluorophore. Every dye has a characteristic fluorescence lifetime. The fluorescence lifetime refers to the average time the molecule stays in its excited state before emitting a photon. This can be used for fluorescence lifetime imaging (FLIM), for example. Here, not a fluorescence intensity picture is plotted, but an image based on the differences in the exponential decay rate of the fluorescence from a fluorescent sample (22).

The fluorescence decay follows an exponential function:

$$[S_1]_t = [S_1]_0 \, e^{-k_F t}$$

Equation 1

where $[S_1]_t$ is the concentration of excited state molecules at time $t$, $[S_1]_0$ is the initial concentration and $k_F$ is the decay rate of the fluorescence or the inverse of the fluorescence lifetime.

The lifetime $\tau$ is defined as:

$$\tau = \frac{1}{k_F}$$

Equation 2

Various radiative and non-radiative processes can de-populate the excited state, as mentioned above. In such cases, the measured lifetime depends on all decay rates:

$$\tau = \frac{1}{k_F + \sum k_{NR}}$$

Equation 3

where $k_{NR}$ is any non-radiative decay rate. A multi-exponential decay has to be assumed if different species exist in a solution or fluorophores change their lifetimes with alternating environment.

### 2.1.3 Quenching of Fluorescence

As already mentioned, there are several processes that inhibit fluorescence. All effects that decrease the fluorescence intensity of a given substance are summarized as *quenching*. Some examples are excited state reactions, energy transfer, complex formation and collisional quenching. In chapter 4.3.3 an example for quenching is given. The fluorescence of the *TAMRA* dye depends upon the chemical environment.

### 2.1.4 Quantum Efficiency

Another important parameter, that combines the previously discussed topics of fluorescence and quenching is the quantum efficiency. The fluorescence quantum efficiency (or quantum yield) $\Phi$ is the ratio of the number of fluorescence photons emitted to the number of photons absorbed during excitation. It represents the ratio of radiative to non-radiative decay and thus the efficiency of the fluorescence process.

$$\Phi = \frac{\#\, of\ emitted\ photons}{\#\, of\ absorbed\ photons} = \frac{k_F}{\sum k_{all\ decays}} = \frac{k_F}{k_F + \sum k_{non-radiative}}$$

**Equation 4**

Another way to define the quantum yield of fluorescence is by the rates of excited state decay, as shown in Equation 4.

## 2.2 Fluorescence Resonance Energy Transfer

Fluorescence or Förster Resonance Energy Transfer (FRET) is the radiationless transfer of energy of an excited fluorophore (donor) to a second fluorophore (acceptor). The basic requirement for FRET is an overlap of the acceptor’s absorption spectrum and the donor’s fluorescence emission spectrum (see Figure 4).

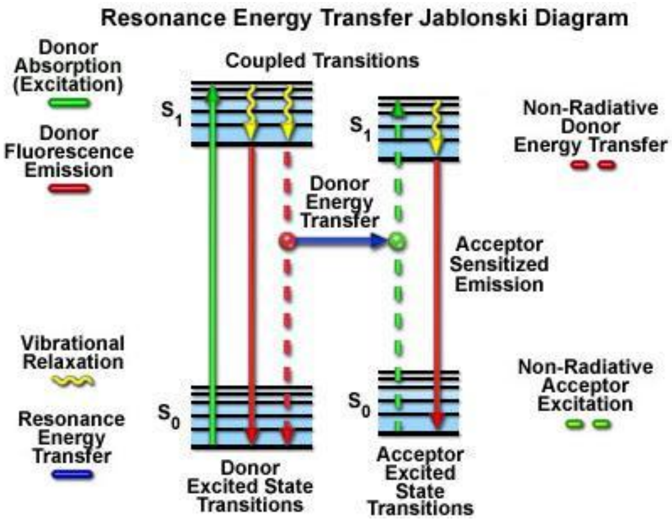
Resonance Energy Transfer Jablonski Diagram
Donor Absorption (Excitation)
Donor Fluorescence Emission
Vibrational Relaxation
Resonance Energy Transfer
Coupled Transitions
$S_1$
$S_1$
$S_0$
$S_0$
Donor Energy Transfer
Acceptor Sensitized Emission
Non-Radiative Donor Energy Transfer
Non-Radiative Acceptor Excitation
Donor Excited State Transitions
Acceptor Excited State Transitions

Figure 5: Simplified Jabloski diagram for FRET: another decay pathway occurs for the excited donor, if a second dye is present. The energy is transfered to the lower-energetic acceptor and can be detedted by measuring the emission of acceptor fluorescence. [Figure adapted from www.microscopyu.com]

The energy transfer occurs due to long-range dipole-dipole coupling (23) and is analogous to a long wave radio, because the radius of interaction is much smaller than the wavelength of light used. When both molecules are fluorescent, the term "fluorescence resonance energy transfer" is often used, although the energy is not actually transferred by fluorescence. Thus, the name "Förster resonance energy transfer" may be preferred. It is named after the German scientist Theodor Förster (11). He treated dyes as Hertzian oscillators and was therefore able to give a precise prediction of the energy transfer.

The efficiency varies strongly with the distance between the two dyes, with the overlap of the acceptor’s absorption spectrum and the donor’s fluorescence emission spectrum, with the quantum efficiency of the acceptor and the orientation between the two dipoles. the transfer rate is given as:

$$k_T = \tau_D^{-1}\left(\frac{R_0}{R}\right)^6$$

Equation 5

where $\tau_D$ is the lifetime of the donor fluorophore without an acceptor, $R$ is the distance between the dyes and $R_0$ is the Förster radius. The Förster radius describes the distance between the two dyes at which on average 50% transfer efficiency takes place:

$$R_0^6 = 8.8\,10^{-28}\kappa^2 n^{-4}\phi_D J \text{ in } [\text{Å}]^6$$

Equation 6

where $\kappa^2$ is the orientation factor, $n$ the index of refraction of the solvent, $\phi_D$ the quantum yield of the donor without acceptor and $J$ the spectral overlap integral.

The FRET efficiency is defined as ratio of transferred photons to photons absorbed by the donor:

$$f_E = \frac{k_T}{\tau_D^{-1} + k_T} = \frac{1}{1 + \left(\frac{R}{R_0}\right)^6}$$

Equation 7

The following figure shows the behaviour of the FRET efficiency of some dye pairs:

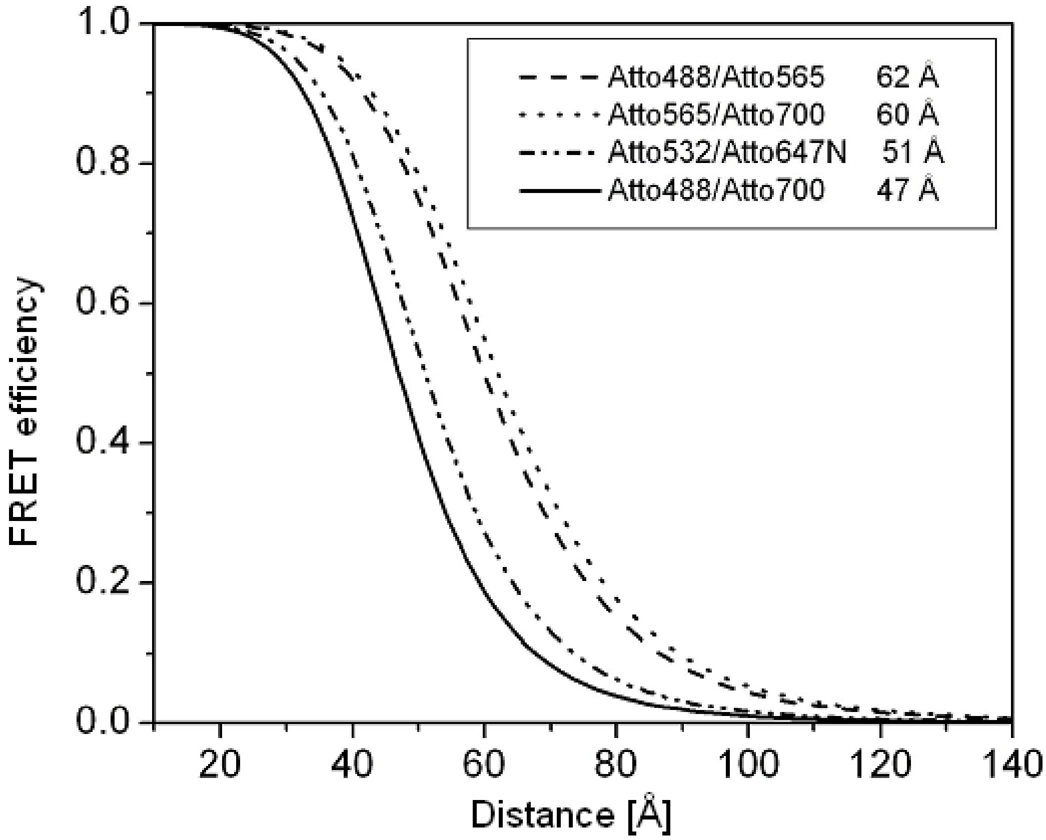

Figure 6: FRET efficiency shown against distance of two dyes in [Å]. [Figure taken from (24)]

How FRET-efficiencies are calculated, is shown in chapter 3.

In biochemical investigations, the most common applications of FRET are the measurement of distances between two sites on a macromolecule (usually a protein or nucleic acid) or the examination of *in vivo* interaction between biomolecular entities. Proteins can be labeled with synthetic fluorochromes or immunofluorescent fluorophores to serve as the donor and acceptor, but advances in fluorescent protein genetics now enable researchers to label specific target proteins with a variety of biological fluorophores having differing spectral characteristics

Although various methods are available for the measurement of FRET in the optical microscope, none are completely without disadvantages. Some techniques require more elaborate and expensive instrumentation, while others are based on assumptions that must be carefully validated. Certain approaches are appropriate for fixed specimens, but cannot be applied to living cell systems while other methods must incorporate significant corrective calculations or data analysis algorithms. It is certain, however, that FRET analysis shows great promise for further development in the utility and scope of biological applications.

## 2.3 Fluorescence Anisotropy

In general, fluorescence anisotropy investigates the rotational diffusion of a molecule from the decorrelation of polarization in fluorescence, i.e., between the exciting and emitted (fluorescent) photons (25). This decorrelation can measure the "tumbling time" of the molecule as a whole, or of a part of the molecule relative to the whole.

The steady-state anisotropy of fluorescence of any colour is formally given by

$$r = \frac{\int_0^\infty r(t)F(t)dt}{\int_0^\infty F(t)dt}$$

Equation 8

where

$$r(t) = \frac{F_\parallel(t) - F_\perp(t)}{F_\parallel(t) + 2F_\perp(t)}$$

Equation 9

is the time-dependent anisotropy, and $F_\parallel(t)$ and $F_\perp(t)$ are the fluorescence detected with a polarization parallel and perpendicular to that of the excitation light, respectively. $F(t) = F_\parallel(t) + 2F_\perp(t)$ is the total fluorescence intensity.

## 2.4 Confocal Microscopy

Confocal microscopy offers several advantages over conventional widefield optical microscopy including the ability to control depth of field and elimination or reduction of background information away from the focal plane (see Figure 7). The principle of Confocal Microscopy was patented by Marvin Minsky in 1957 (7).

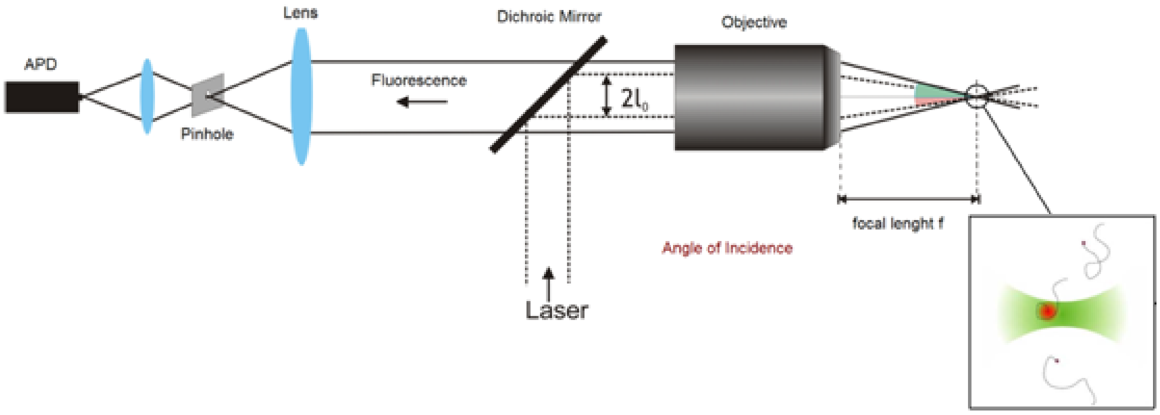

Figure 7: Schematically beam path in confocal microscopy. [Picture adapted from (24)]

In a conventional widefield microscope, the entire specimen is bathed in light from a mercury or xenon source, and the image can be viewed directly by eye or projected onto an image capture device or photographic film. In contrast, the method of image formation in a confocal microscope is fundamentally different. One or more lasers are coupled into the back aperture of the objective by a dichroic mirror and are focused into the sample, which is liquid in our case. The fluorescence of this sample is collected with the same objective and focused on a pinhole, that cuts of out-of-focus light. Subsequently, the fluorescence is focused onto an avalanche photodiode.

# Chapter 3: Theory of Analysis Methods

## 3.1 Pulsed Interleaved Excitation

In a multi-colour experiment, it is not only important to know in which detection channel the photon arrives, but also the corresponding excitation source, responsible for generating the fluorescent photon. This is realized with Pulsed Interleaved Excitation (PIE) (20). PIE is intrinsic in the setup, but needs to be explained beforehand since it is important for the subsequent analysis methods.

PIE requires the use of two or more pulsed excitation wavelength. These alternate with sufficient time delay, that all emitted photons from one laser pulse are detected before the next pulse of a different colour arrives. In our case a green and a red laser are used (see Figure 8), which are synchronised to a master clock. The second laser is delayed approximately 20 ns with respect to the first one (see Figure 25). The repetition rate used in this setup is $26,\overline{6}$ MHz. Usually, fluorescence decay times are in the range of 2-10 ns. This means the probability of allocating a photon to the incorrect excitation source is < 0.1%.

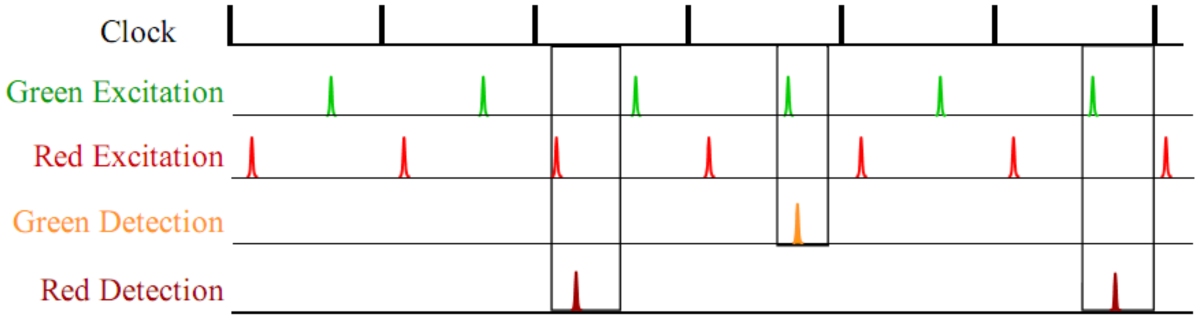

Figure 8: Schematic illustration of Pulsed Interleaved Excitation [Adapted from (24)]

During one cycle, the red and the green lasers illuminate the sample consecutively. After each excitation, the photons are collected in the green and the red detection channel. In addition to the detection channel, the arrival time of the photon is saved in terms of clock cycles (macro time) and also with ps resolution relative to the clock pulse (TTTR) (micro time).

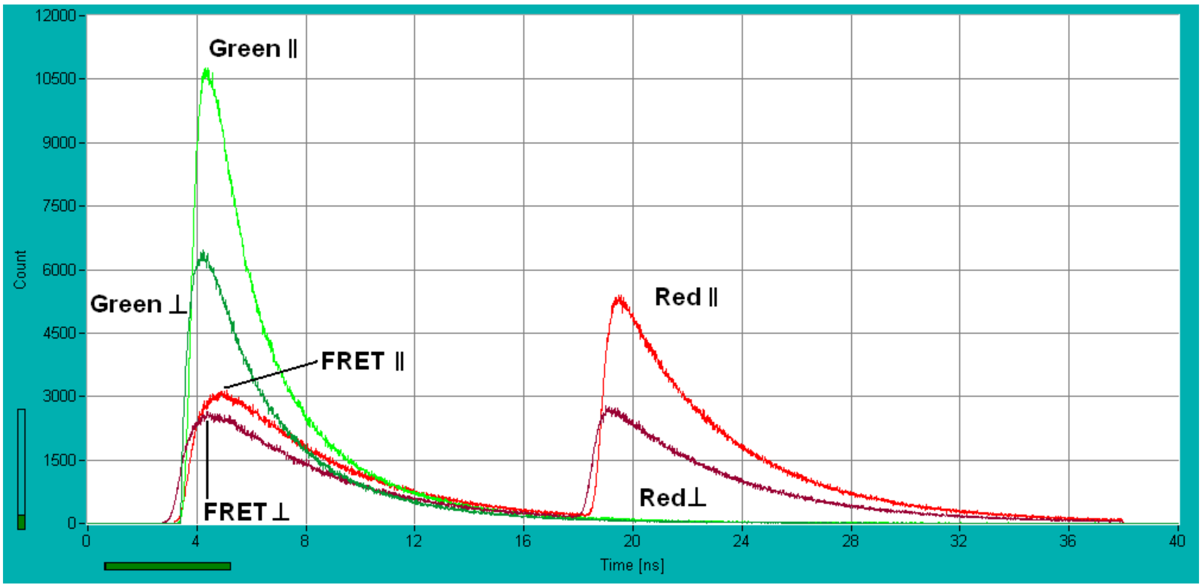

**Figure 9: Lifetime histogram of a high FRET DNA sample shown for all four detection channels (red = red detection channel and green = green detection channel; dark colour = ⊥, light colour).**

A histogram over all clock cycles is shown in Figure 9. Each photon is plotted with respect to its arrival time relative to the master clock pulse. The master clock frequency is 26.7 MHz, thus resulting in a length for one cycle of 37.5 ns. Figure 9 also points out the limitation of PIE. The delay between the laser-pulses must be large enough so that the fluorescence of one dye vanishes before the next excitation pulse arrives.

The photons within each detection channel can be separated by their excitation source, which results in a total of four channels for each polarization: green detection after green excitation ($F_{GG}$), green detection after red excitation ($F_{GR}$), which is energetically not possible, red detection after red excitation ($F_{RR}$) and red detection after green excitation ($F_{RG}$). The diagram of all four channels for one polarization after a measurement can be seen in Figure 10.

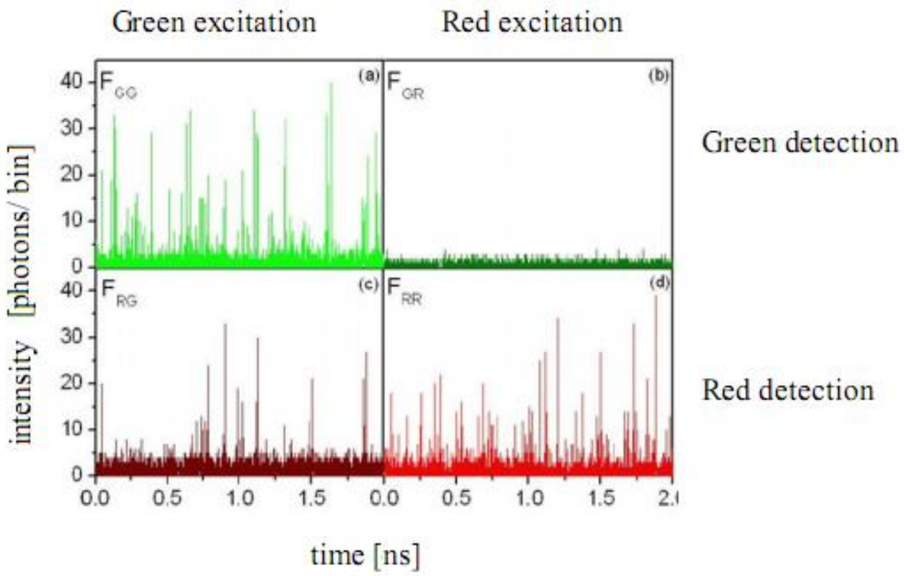

**Figure 10: The four channels available with PIE : (a)green detection after green excitation ($F_{GG}$), (b) green detection after red excitation ($F_{GR}$), (c) red detection after green excitation ($F_{RG}$) and (d) red detection after red excitation ($F_{RR}$). A *bin* is a time segment with the length of individual choice, where all arriving photons are summed up.**

The channel with green detection after red excitation is not completely empty, although red light is not able to excite the green fluorophore. When scattered light is excluded from the green channel with the right set of filters, the count rate in the $F_{GR}$ channel is only that of the dark counts from the detector.

PIE hereby provides the information of which excitation source generated each detected fluorescence photon. The applications for PIE are versatile. One already mentioned application of PIE is the differentiation of molecules that are labelled with acceptor and donor fluorophore from molecules that have just one dye attached (see chapter 3.3). In addition, PIE can be used with three or more excitation sources (26), where it is possible to determine distances between several fluorophores simultaneously. But also the techniques like 2D PCH (27) and 2D-FIDA (Kask 1999) benefit from the use of PIE.

## 3.2 Fluorescence Correlation Spectroscopy

Fluorescence Correlation spectroscopy (FCS) was introduced in the 1970's (28) (29) (30) and is nowadays a common technique to experimentally characterize the dynamics of fluorescent species. Light is focused on a sample and the measured fluorescence intensity fluctuations (due to diffusion, physical or chemical reactions, aggregation, etc.) are analyzed using the temporal autocorrelation. To measure such small fluctuations, it is helpful, but not mandatory to operate with volumes as small as possible and concentrations that are near to an optimum measurement regime at the level when individual species enter or exit the observation volume. When too many entities are measured at the same time, the overall fluctuations are small in comparison to the total signal and may not be resolvable - in the other direction, if the individual fluctuation-events are too sparse in time, it becomes impossible to get good statistics in a single measurement. When a molecule diffuses through the confocal volume, it is excited by the laser and emits fluorescence photons. Hence the photons are not detected randomly but in bursts that depend on the trajectory the molecule takes through the volume. By correlation analysis, it is possible to extract the characteristic and underlying processes that lead to these fluctuations.

### 3.2.1 Autocorrelation

The (temporal) autocorrelation function (ACF) is the correlation of a time series with itself, shifted by time τ, as a function of τ.

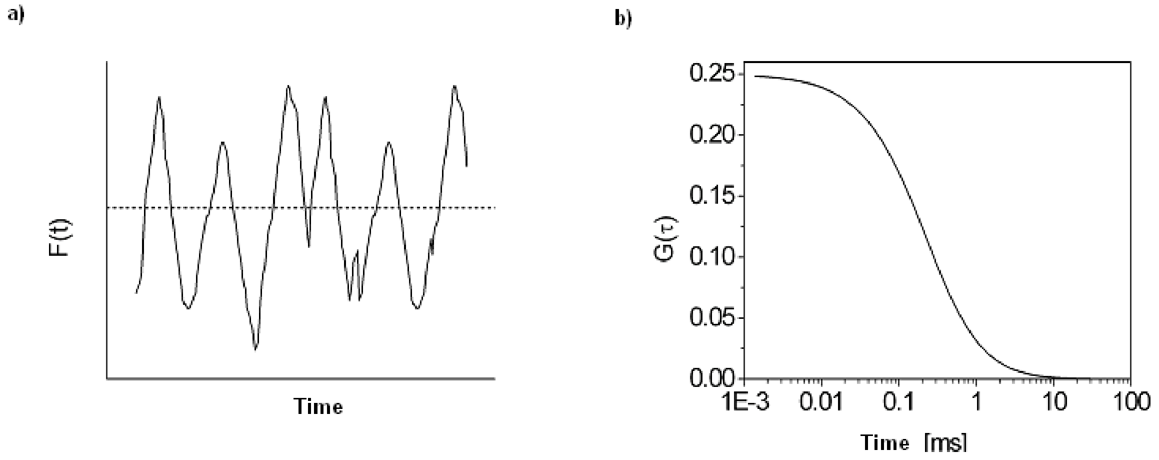

Figure 11: Fluorescence Correlation Spectroscopy: (a) The autocorrelation of the fluctuations of the fluorescence signal results in an autocorrelation function, shown in (b). For freely diffusing species, the height of the autocorrelation function is inversely proportional to the number of particles in the confocal volume and the decay to half of the amplitude provides information about the mobility of the fluorescent molecule.

The autocorrelation function that describes the self-similarity of a fluctuating signal can be calculated as the product of signal at a certain time *t* with the signal at the time $t+\tau$. For the calculation of the ACF, freely and non-interacting species are assumed. The detection volume is approximated as three-dimensional Gaussian:

$$G_{DIFF}(\tau) = \frac{2^{-3/2}}{\langle N \rangle} \left( \frac{1}{1+\frac{4D\tau}{\omega_r^2}} \right) \left( \frac{1}{1+\frac{4D\tau}{\omega_z^2}} \right)^{1/2}$$

Equation 10

where $\langle N \rangle$ is the averaged number of particles in the effective confocal volume, *D* is the diffusion coefficient and $\omega_r$ and $\omega_z$ are the sizes of the confocal volume in the x/y-plane and in z-direction, respectively.

Visually speaking, the ACF gives the probability of detecting a photon (above the average countrate) at the time $t+\tau$ when one has already been detected at time *t*.

The ACF gives direct information about two parameters: first, the number of particles within the confocal volume. With supplementary knowledge about the size of the confocal volume, the number of particles can be converted into concentration. This is done by:

$$G(0) = \frac{2^{-3/2}}{V \cdot \langle C \rangle \cdot N_A} \Longleftrightarrow \langle C \rangle = \frac{2^{-3/2}}{V \cdot G(0) \cdot N_A}$$

Equation 11

The effective size of the volume is given by $V = (\pi/2)^{1.5}\omega_r^2\omega_z$. The factor of $(\pi/2)^{1.5}$ accounts for the difference between an infinite three-dimensional gaussian and a defined, uniformly illuminated volume.

The second parameter in the ACF is the diffusion coefficient, which can be derived from the Einstein-Stokes-relation (31) (32) (33). For spherical particles applies:

$$D = \frac{k_B T}{6\pi\eta R_h},$$

Equation 12

where $k_B$ is the Boltzmann constant, *T* the temperature, $\eta$ the viscosity of the solvent and $R_h$ the hydrodynamic radius. The diffusion time $\tau_D$ is then given by:

$$\tau_D = \frac{\omega_0^2}{4D}.$$

Equation 13

The diffusion coefficient reveals the averaged dwell time within the confocal volume. One has to keep in mind that the calculated $\tau_D$ is still convoluted with the detection optics. With an infinite detection volume in the z-direction, $\tau_D$ would exactly correspond to a decay of the ACF to the half of its height.

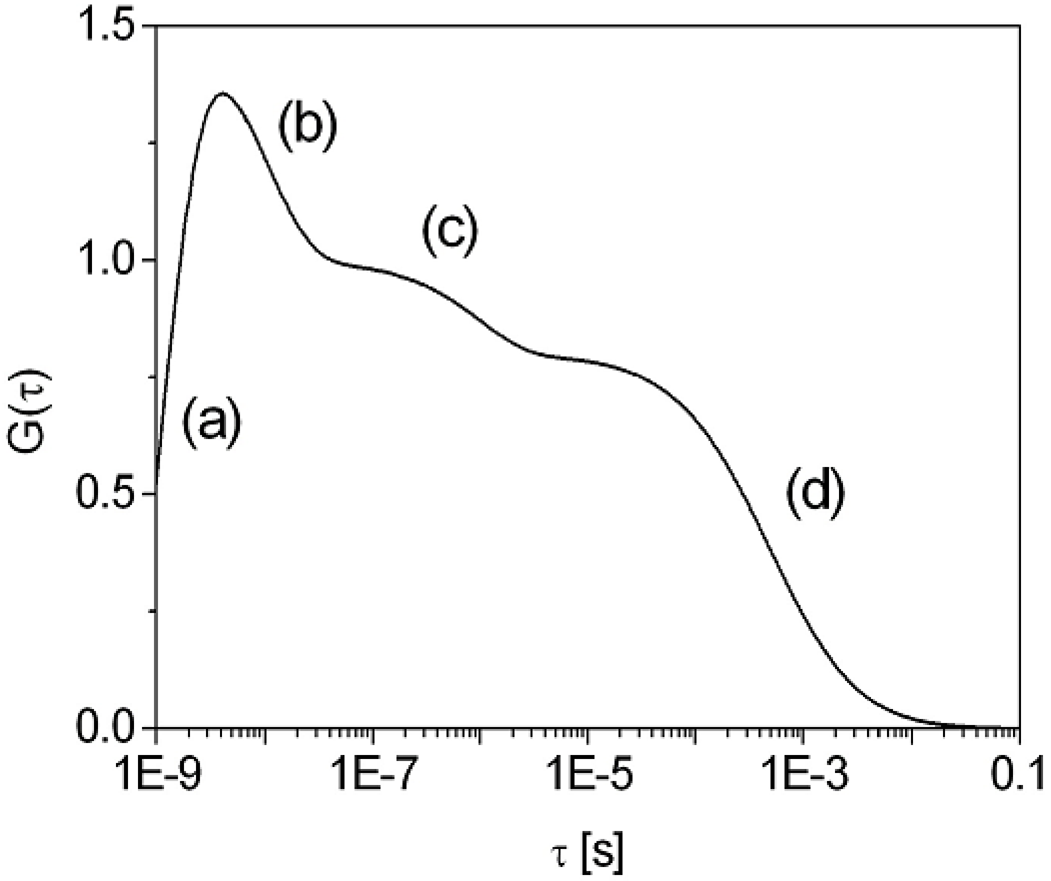

Figure 12: The Autocorrelation function: different processes occur at different time scales: (a) antibunching - emerges because the fluorophore has to be excited again before emission of a second photon. Antibunching is usually not observable due to dead time of detectors (b) rotational diffusion (c) intra-molecular reactions like transition from the singlet to the triplet state (d) translational diffusion

FCS is sensitive to changes in the molecular brightness - the counts per molecule per micro-watt. So it is possible, additionally to the already mentioned parameters, to investigate other processes like rotational diffusion, directed transport, intra-molecular dynamics and conformational changes. This is feasible because all these processes take place on different time scales as shown in Figure 12. The application of FCS is discussed in chapter 5.2.

### 3.2.2 Cross-Correlation

Theoretically, it is possible to resolve any bimolecular reaction of a freely diffusing fluorophore with FCS due to the change in molecular weight and diffusion coefficient. However, the sensitivity of the ACF is limited because of the diffusion coefficient's dependency on the hydrodynamic radius and therefore changes are incorporated with the cubed root of the molecular weight.

Eigen and Rigler suggested labelling two different components of the reaction with different dyes (Eigen M 1994). When a double-labelled molecule passes the overlapping confocal volumes of dual-colour excitation, then a burst of photons appears in both detection channels. These two fluorescence signals are correlated. As already mentioned, the ACF compares a signal with itself to reveal repeating processes. The cross-correlation function (CCF) analyzes the similarities of two different signals. The technique is called Fluorescence Cross-Correlation Spectroscopy (FCCS) and is perfectly suited to investigate interactions where two components react or a species separates into two.

The CCF of channel *i* and *j* is given as

$$G(\tau)_{i\,x\,j} = \frac{\langle \delta F_i(t)\delta F_j(t+\tau)\rangle}{\langle F_i(t)\rangle\langle F_j(t)\rangle}$$

Equation 14

For translateral diffusion, the CCFs are symmetric, so $G_{i\,x\,j}$ and $G_{j\,x\,i}$ are identical and typically averaged. When the molecular brightness of each individual component stays constant regardless the reaction state, then the fluorescence signals of two different species (G) and (R) can be written as:

$$F_G(t) = \int W_G(\vec{r}) \cdot\ \varepsilon_G[C_G(\vec{r},t) + C_{GR}(\vec{r},t)]\, d\vec{r}$$

Equation 15

$$F_R(t) = \int W_R(\vec{r}) \cdot\ \varepsilon_R[C_R(\vec{r},t) + C_{GR}(\vec{r},t)]\, d\vec{r}$$

Equation 16

where $W_i(\vec{r})$ is the probe volume of the *i*th species, $C_i(\vec{r},t)$ its concentration and $C_{GR}(\vec{r},t)$ the concentration of double-labelled particles.

When the volumes are identical in size and shape and completely overlap, the CCF is given by (34):

$$G_{G\,x\,R}(\tau) = \frac{2^{-3/2} N_{GR}}{\langle N_G + N_{GR}\rangle\langle N_R + N_{GR}\rangle}\left(\frac{1}{1+\frac{4D_{GR}\tau}{\omega_r^2}}\right)\left(\frac{1}{1+\frac{4D_{GR}\tau}{\omega_z^2}}\right)^{1/2}$$

Equation 17

The CCF is indirect proportional to the number of double labelled particles when the total number of particles remains constant. The number of double-labelled molecules in the volume and therefore the concentration can be calculated, using:

$$\langle C_{GR}\rangle = \frac{G_{G\,x\,R}(0)}{V \cdot G_G(0) \cdot G_R(0)}$$

Equation 18

One problem of FCCS is that the confocal volumes are not identical in size or position due to chromatic aberrations. Perfect overlap is also very difficult to realize, but due to way our setup is build, this could be avoided (see chapter 5).

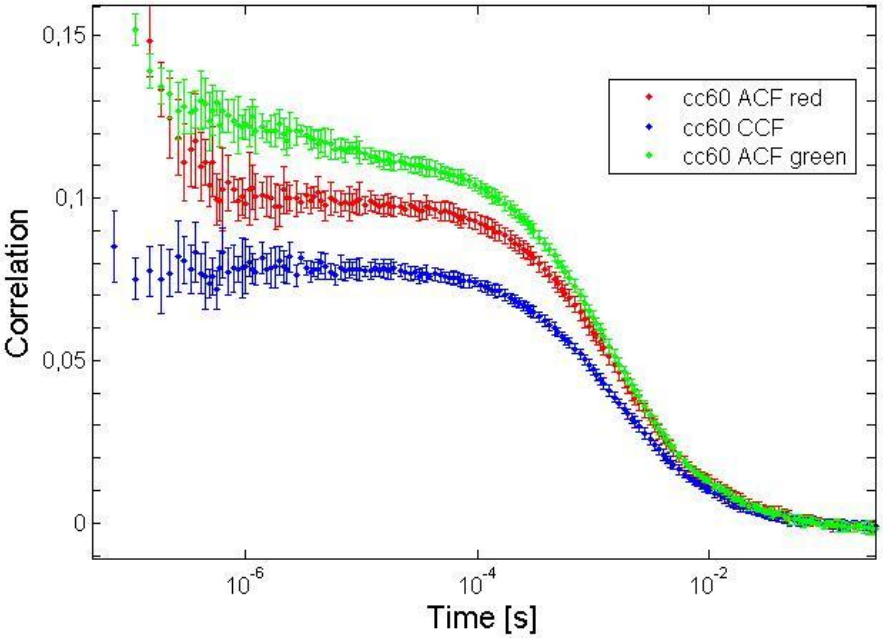

Figure 13: ACFs of green and red detection channel, respectively, and the corresponding CCF of the CC60 DNA

Figure 13 shows the green and red ACFs and the CCF of a 60 base pair DNA that is labelled with Atto532 and Atto647N (AttoTec, Siegen, Germany) at both ends, respectively. The structure of both dyes is shown below, just recently published by (35).

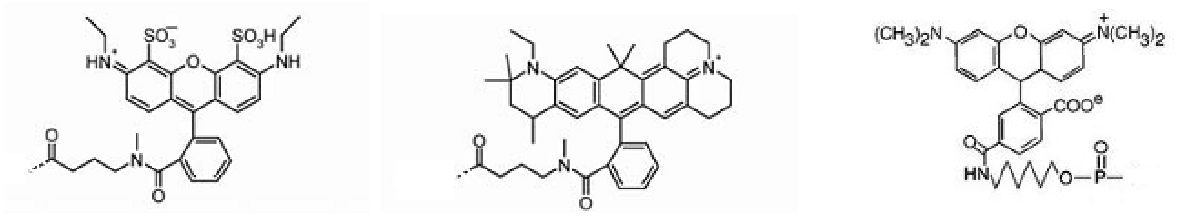
SO3⁻
SO3H
HN
NH
O
N
O
N
N
O
N
O
(CH3)2N
O
N(CH3)2
COO⁻
O
HN
O–P–
O

Atto532 Atto647N TAMRA

Figure 14: Structure of the dyes used in this work. The structure of Atto550 is still unknown.

Yet another dye was used in combination with HSP90 (see chapter 4.2), Atto550 (AttoTec, Siegen, Germany). The structure of this dye has not been published yet.

## 3.3 Burst Analysis

In this work, the technique of Burst Analysis was used to determine single molecule FRET efficiencies. For this purpose, samples are measured that have a concentration of several tens of pM. Due to Brownian movement, the single or double labelled molecules diffuse through the confocal volume, as shown in Figure 15. During their way through the volume, they emit a burst[1] of photons. The number of photons within a bin depends on the duration of stay of the single molecules in the volume. The concentration is kept very low to minimize the probability of having two molecules in the focus at the same time.

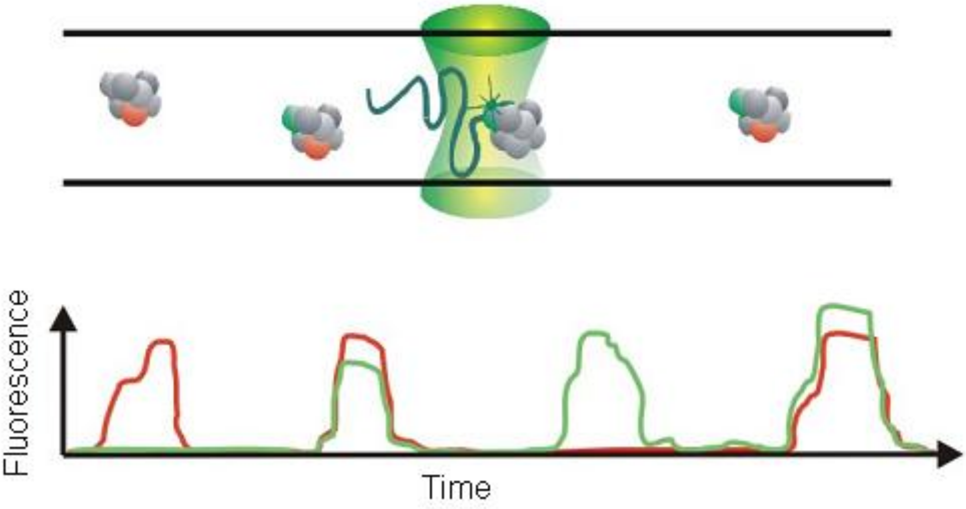

Figure 15: Differently labelled molecules result in different detection signals. Concentration is kept in the pico-molar range to keep the possibility of having two molecules in the confocal volume insignificant. [Adapted from (24)]

Typically in an single-molecule FRET experiment just the donor is excited by a continuous wave laser (cw laser) but donor and acceptor fluorescence are detected. A burst of photons is counted as burst when the sum of both channels reaches a certain threshold. For these events, the FRET efficiency $f_E$ can be calculated as fluorescence-intensity of the acceptor ($F_A$) divided by the total fluorescence-intensity. The total fluorescence-intensity consists of the fluorescence of the acceptor ($F_A$) and the donor ($F_D$), which has to be adjusted with the correction factor $\gamma$:

$$f_E = \frac{F_A}{F_A + \gamma F_D}$$

Equation 19

---

[1] An accumulation of photons within one time bin is referred to as burst

$\gamma$ represents hereby the different detection efficiencies[2] and quantum yields of the two fluorophores (36). This factor is the ratio of the product of detection efficiency $\eta$ and quantum yield $\Phi$ of acceptor and donor, respectively:

$$\gamma = \frac{\eta_A \Phi_A}{\eta_D \Phi_D}$$

Equation 20

PIE has a strong influence on the distribution of FRET efficiencies. PIE eliminates the FRET efficiencies around zero that belong to donor-only species. With a continuous laser, one would detect two channels ($F_{Donor}$ and $F_{acceptor}$), but PIE allows determination of the excitation source as well, as shown in Figure 8: Schematic illustration of . Figure 16 visualizes the criteria that are necessary to calculate FRET efficiencies.

To extract the correct FRET values out of the measurement, two sources for errors have to be eliminated: the first is the spectral crosstalk of the donor fluorophore, i.e. green fluorescence that is recorded in the red detection channel, and the second is direct excitation of the acceptor dye with the donor laser. Both terms are measured beforehand for each pair of donor and acceptor and the average is then taken into account. This leads to the modified form of Equation 21 (37):

$$f_{E=} = \frac{F_A - \beta_{DIR} F_{Aonly} - \beta_{CT} F_D}{F_{AD} - \beta_{DIR} F_{Aonly} - \beta_{CT} F_D + \gamma F_D}$$

Equation 21

where $F_A$ and $F_D$ are the fluorescence intensities of the acceptor and donor channels, respectively , $\beta_{DIR}$ the relative ratio of direct excitation, $\beta_{CT}$ the relative ratio of crosstalk and $F_{Aonly}$ is the intensity of the acceptor only, that has to be measured without donor.

The FRET efficiency can be converted into distance by:

$$R = R_0 \left(\frac{\gamma F_D}{F_A}\right)^{1/6}$$

Equation 22

With Burst Analysis it is possible to measure exact FRET values that are not averaged over all efficiencies and therefore it is possible to make dynamics of the sample visible.

---

[2] The detection efficiency is a combination of the sensitivity of the detectors at the corresponding wavelength and the filters/dichroic mirrors that are used in the setup

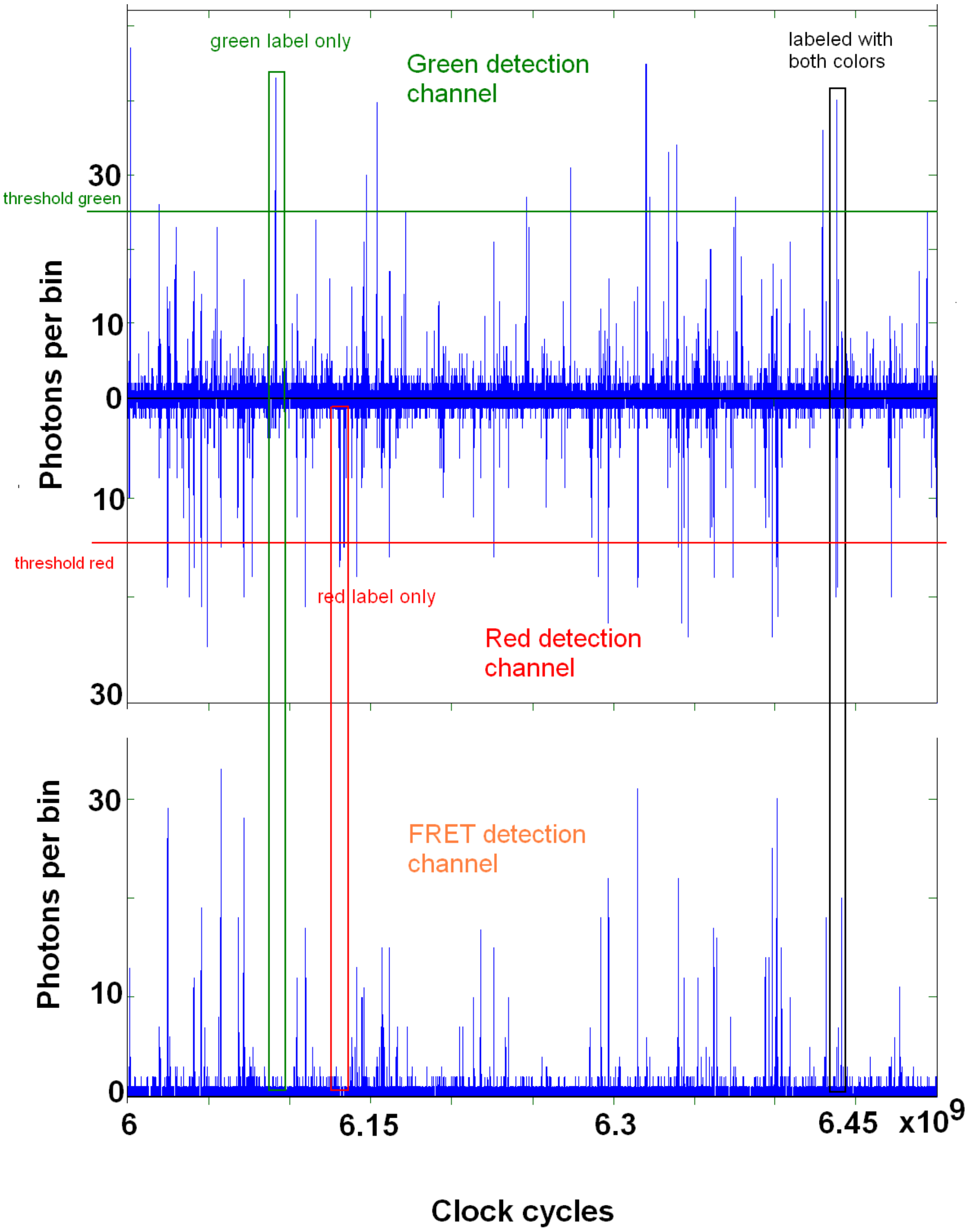

Figure 16: Binned count rates of green (top), red (middle) and FRET (bottom) detection channel. With PIE not only a total threshold (donor criterion) has to be applied but also the amount of red photons with red excitation has to come over a threshold (acceptor criterion). Only if bursts appear simultaneously after red and green excitation, FRET efficiencies are calculated. Each clock cycle has the duration of 37 ns.

Another interesting application of PIE is the determination of the stoichiometry of a sample (38) in combination with the FRET efficiencies, that are calculated with burst analysis. The stoichiometry describes the ratio of green to total intensity:

$$S = \frac{F_{GG} + F_{RG}}{F_{GG} + F_{RG} + F_{RR}}$$

Equation 23

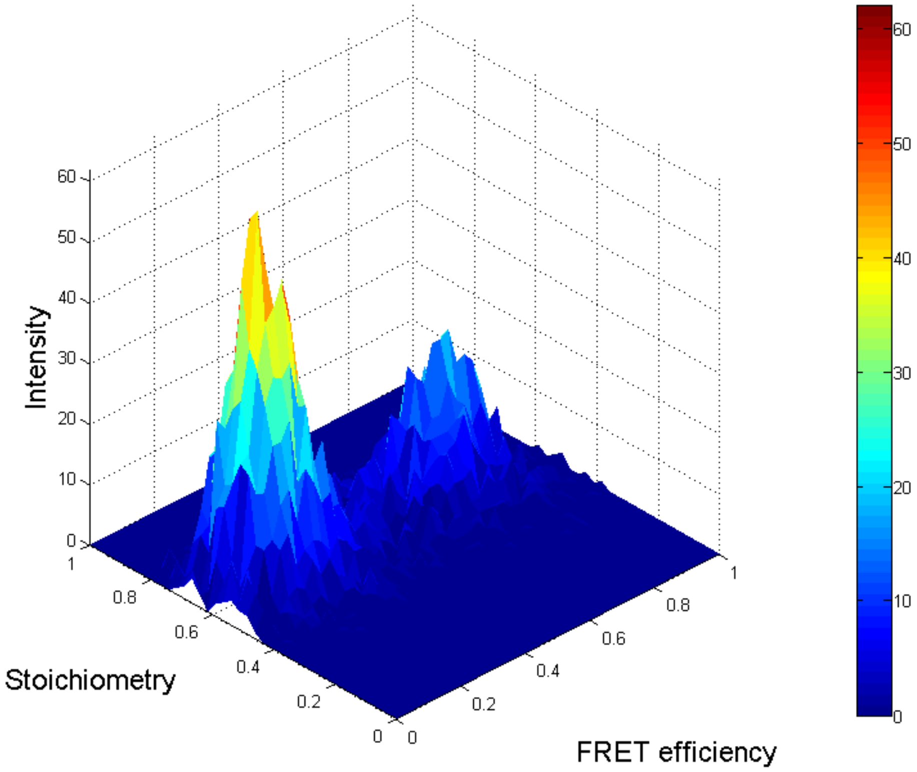

Figure 17: Stoichiometry versus FRET efficiency plot of a high- and a low-FRET species

Figure 17 shows the stoichiometry plotted against the FRET efficiency of a mixture of high-FRET DNA (~0.8, b2d1) and a low-FRET DNA (~0.1, b3d4). A stoichiometry of approximately 0.5 means a ratio of donor to acceptor of 1:1. The stoichiometry depends on the laser excitation intensities.

The stoichiometry allows to distinguish if molecules possess a different ratio of acceptor- to donor-fluorophores. This can either serve as control, when a sample should only contain one ratio of labels, or it serves as analysis method for identification of several different species in one solution.

# Chapter 4: Results and Discussion

## 4.1 Mutiparameter Setup

### 4.1.1 Configuration of the MPF-Setup

During this work, a four-channel setup based on a Nikon TE300 (Nikon, Tokyo) inverted microscope was constructed. The whole system is mounted upon a optical table (Melles Griot , Albuquerque, USA). A schematic drawing of the optical and electrical paths is shown below.

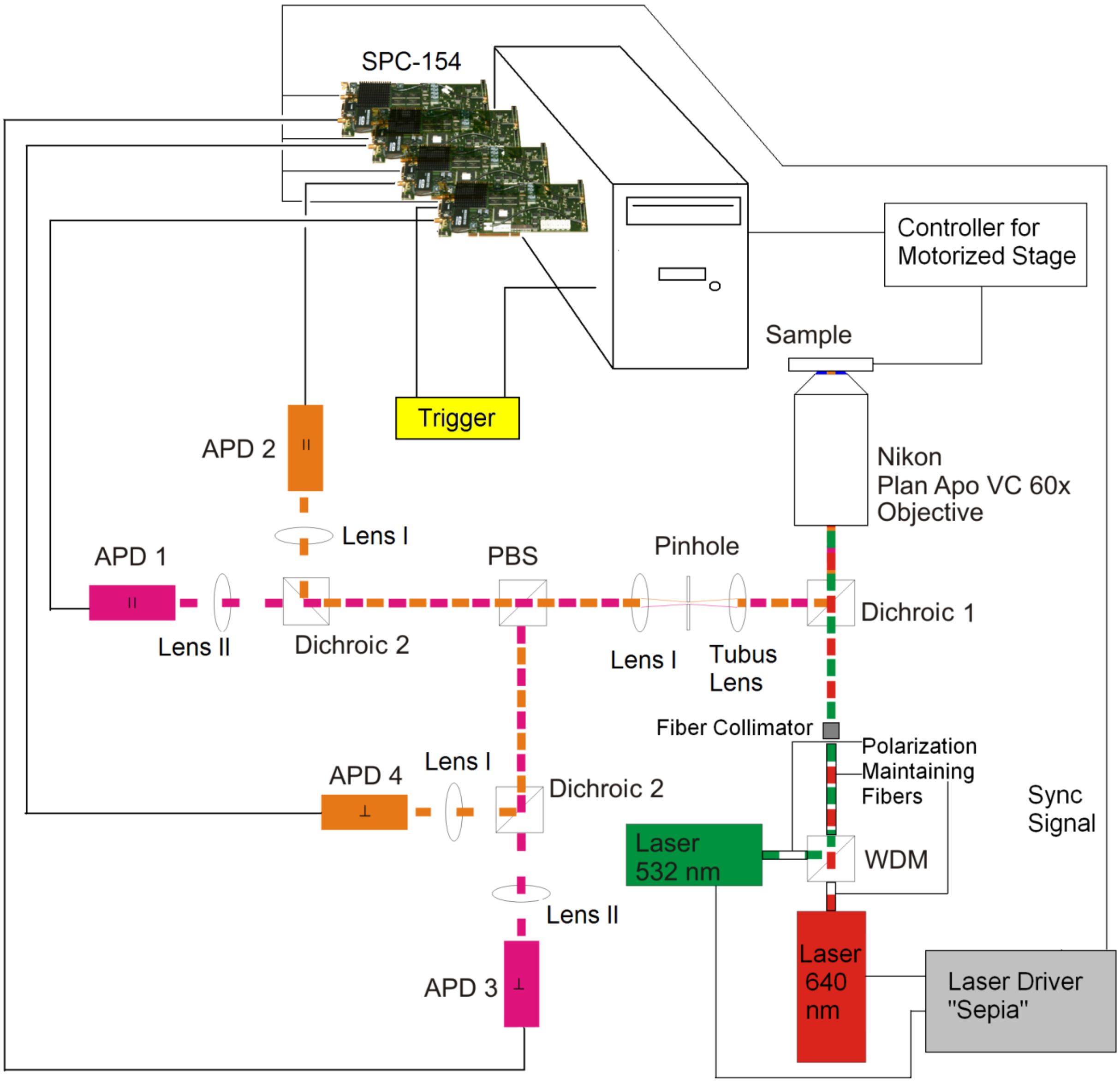
SPC-154
Controller for Motorized Stage
Sample
Trigger
APD 2
Nikon Plan Apo VC 60x Objective
Lens I
APD 1
PBS
Pinhole
Dichroic 1
Lens II
Dichroic 2
Lens I
Tubus Lens
Fiber Collimator
Polarization Maintaining Fibers
Sync Signal
Lens I
APD 4
Dichroic 2
Laser 532 nm
WDM
Lens II
Laser 640 nm
Laser Driver "Sepia"
APD 3

Figure 18: A schematic drawing of the MPF-setup

Two pulsed laser diodes serve as light sources. One is a PicoTA 530 (PicoQuant and Toptica, Berlin) which produces laser pulses shorter than 100 pico-seconds at full-width-half-maximum (FWHM) and emits at 1060 nm but is frequency doubled to 530nm, using a second-harmonic generation module. The maximum power is approximately 2 mW at a repetition rate of 40 MHz. The other laser is a LDH-D-C-640 (PicoQuant, Berlin), operable in either cw or pulsed mode. The pulses are shorter than 90 ps (FWHM) with a maximum output of 1.5 mW. Pulsed diode lasers unfortunately suffer the disadvantage that with rising power a tail in the laser pulse emerges and the Gaussian shape vanishes. This is shown in Figure 19:

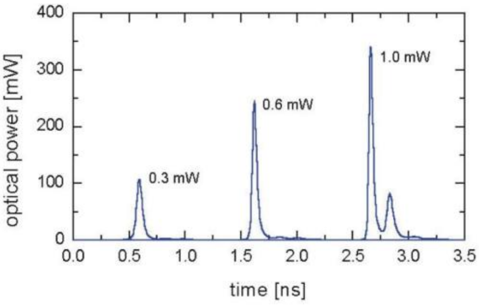

Figure 19: Changing shape of Laser pulse with increasing power

The pulses are generated in a Multichannel Picosecond Diode Laser Driver "Sepia" (PicoQuant, Berlin). This driver allows adjusting the frequency (10.0 - 80.0 MHz) of the pulses as well as the total laser intensity. In this setup, a laser repetition rate of 26.7 MHz was used.

Both Lasers are directly fiber-coupled into polarization-maintaining, single-mode fibers (Schäfter+Kirchhoff, Hamburg). The fibers are connected to a Wavelength Division Multiplexer (AMS Technologies, Martinsried, Germany) that acts in our case as beam combiner and joins both laser-beams into one polarization-maintaining single-mode fiber (AMS Technologies, Martinsried, Germany). The output of the fiber is connected into a fiber collimator (60FC-4-RGB11-47, Schäfter+Kirchhoff, Hamburg) that is especially designed for confocal microscopy with minimal dispersion and aberration in the range of 408 to 660 nm.

The beam is directed into the rear part of the microscope by two mirrors with a broadband-coating from 350 to 800 nm (BB1-E02, Thorlabs, Dachau, Germany). The excitation photons are then reflected into the objective by a dichroic mirror (dichroic (1) in Figure 18, z 532/635, AHF Analysetechnik, Tübingen, Germany). The reflection spectrum is shown in Figure 20 (a).

The beam is focused into the sample by a water-immersion objective - Nikon PlanApo VC60x N.A. 1.2 (Nikon, Tokyo). The sample can be moved with a motorized stage that is either controlled manually with the joystick or automatically from the computer (Märzhauser, Wetzlar, Germany).

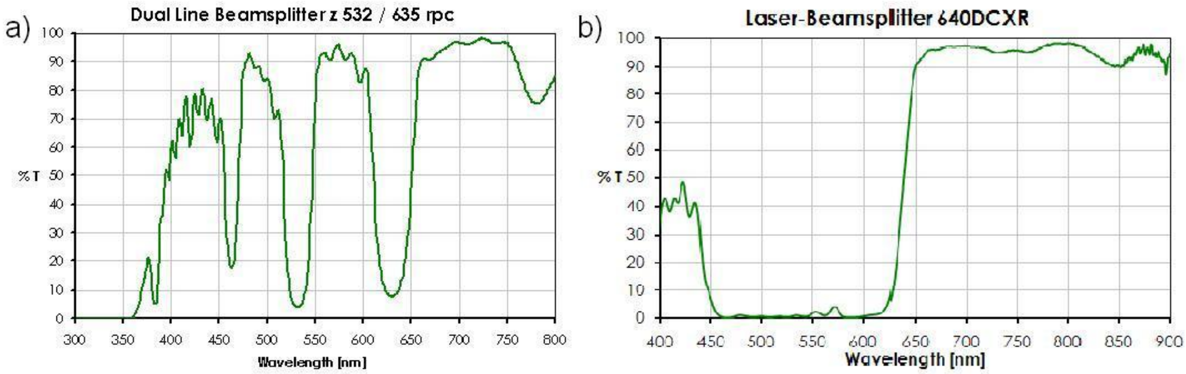

Figure 20: (a) Transmission spectrum of the dichroic mirror in the microscope (1) and (b) transmission spectrum of dichroic mirror (2) in detection path

The fluorescence light is collected by the same objective and passed through the dichroic mirror (1). The tube lens focuses the light through the side-port of the microscope onto the confocal pinhole (50 µm, Thorlabs, Dachau, Germany). The focused beam is recollimated by a achromatic lens (Lens (1) Figure 18, AC254-100-A1, Thorlabs, Dachau, Germany) to a beam diameter of approximately 3 mm and guided to a Polarizing Beam Splitter Cube (PBS3, Thorlabs, Dachau, Germany). This cube splits the light into p- and s- polarization as shown in Figure 21. The polarized light is then separated into green and red fluorescence. This is done by dichroic mirrors (2) (laser beamsplitter 640DCXR, AHF analysetechnik AG, Tübingen) that reflect green photons and let red photons pass (Figure 20 (b)).

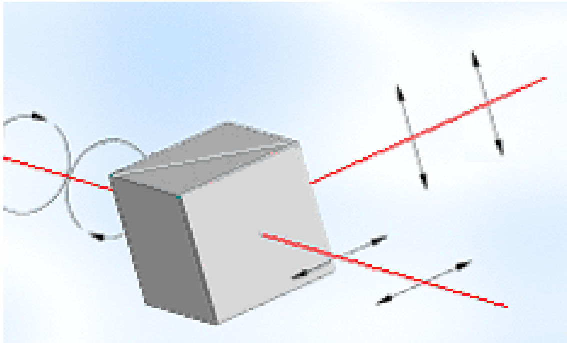

Figure 21: Functionality of a polarizing beam splitter cube

The photons that are now divided by polarization and wavelength pass a emission filter (green: Brightline HC582/75; red: Brightline HQ700/75) to eliminate scattered laser light. With achromatic lenses, (1) (AC254-100-A1, Thorlabs, Dachau, Germany) for green photons and (2) (AC254-100-B, Thorlabs, Dachau, Germany) for red photons, the light in each channel is now focused onto a single-photon-Avalanche-Photodiode (2x SPCM-AQR-14 for red channels and 2x SPCM-AQR-16 for green channels, Perkin Elmer, Fremont, USA). The collected photons are transformed into TTL-pulses and recorded by four TCSPC-cards (SPC-154, Becker & Hickl, Berlin).

Figure 22 shows a schematic drawing of the assembly of the detection pathway. Every photon travels the same distance from the microscope to the detector, regardless of its wavelength or polarization.

An additional camera is attached to the front port for alignment without without visual inspection through the oculars.

For long measurements on multiple samples, a special sample holder made of Teflon has been designed. Contrary to the typically sample holder with a single chamber, this sample cell holds six different samples. In combination with the motorized stage, we were able to follow reactions in six different samples for up to 48 hours. For long measurements, one should avoid using water as immersion medium. The Zeiss Immersion Oil *Immersol W* with a refraction index of 1.33 (at 23°C) is a good alternative due to its low-volatile behaviour.

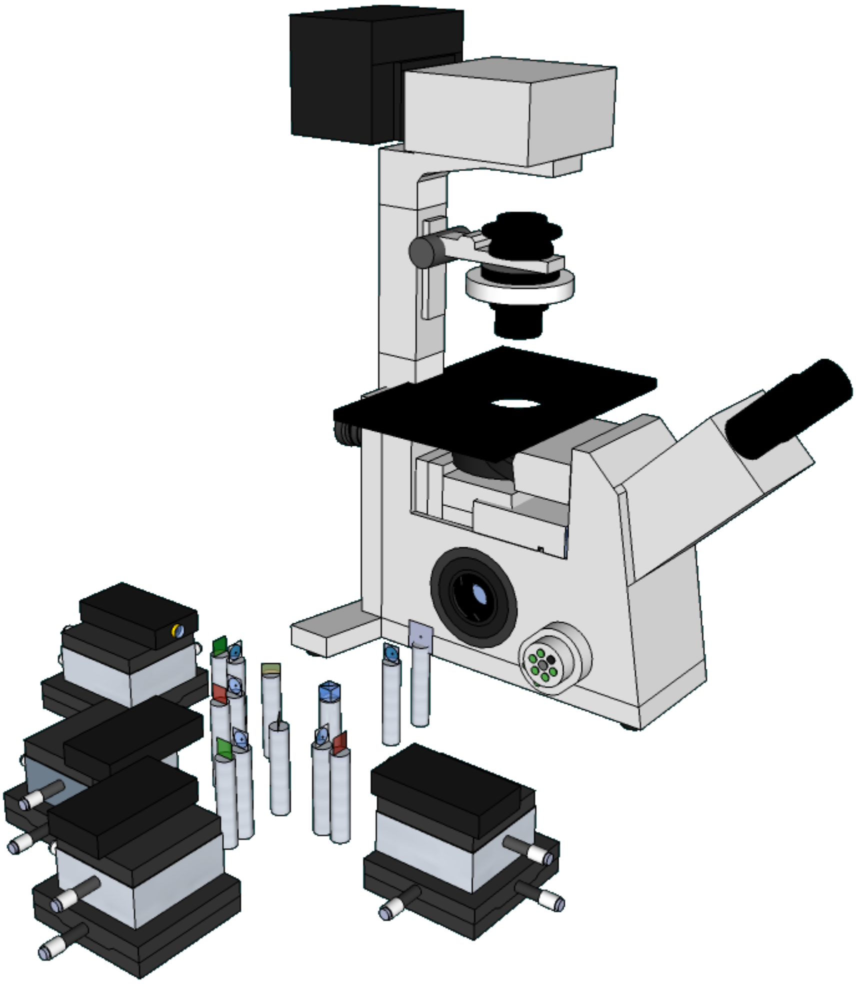

Figure 22: Drawing of the detection pathway

With this setup one is able to distinguish the excitation source, the wavelength, the polarization, the arrival time of every photon and the lifetime of a dye. A detailed insight of the calibration and the characteristics of the setup is given in the next section

## 4.1.2 Characterization of the Setup

### 4.1.2.1 Size of the Green and Red Detection Volumes

To determine the size of the green confocal volume, several FCS measurements of Rhodamin 6G (R6G) are averaged. The diffusion coefficient of Rhodamine 6G, quantified by 2-focus-FCS, is *D(Rh6G)=415±5µm*$^{2}$*s*$^{-1}$ (39). A typical curve is shown below.

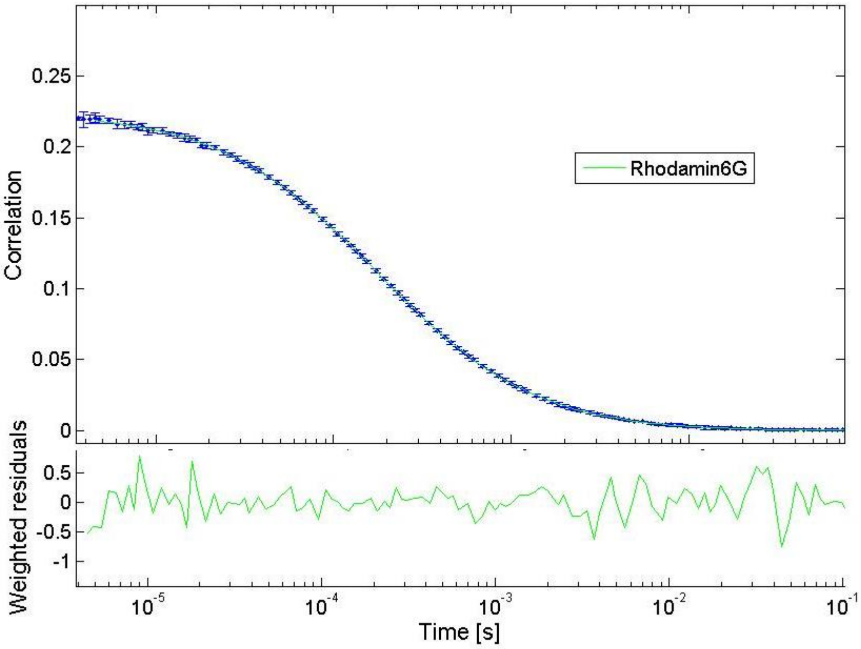

**Figure 23: Typical FCS measurement of Rhodamin6G with fit and weighted residuals for determination of green detection volume**

To calculate the corresponding volume, the diffusion time ($\tau_D$ = *0.19±0.02ms*) and the structure parameter *p* (*p = 7.0±0.5*), defined as the ratio of axial to lateral length of the focus:

$$p = \frac{z_0}{\omega_0}$$

**Equation 24**

needs to be extracted. The lateral parameter, $\omega_0$, can be calculated from rearrangement of Equation 13:

$$\omega_0 = \sqrt{4 \cdot D \cdot \tau_D}$$

$$\omega_{0G} = (535 \pm 20\,)nm$$

The effective confocal volume, for the green channel is the calculated using:

$$V = \left(\frac{\pi}{2}\right)^{3/2} \omega_0^2 z_0.$$

Equation 25

In combination with Equation 24, the following transformation is possible:

$$V = \left(\frac{\pi}{2}\right)^{3/2} \omega_0^3 p$$

Equation 26

$$V_G = (2.12 \pm 0.37) \cdot 10^{-15} L.$$

In the same manner the confocal volume for the red channel is calculated. For this purpose several FCS measurements with the dye Cy5 ($D = 370\ \mu m^2 s^{-1}$, (39)) were acquired and averaged.

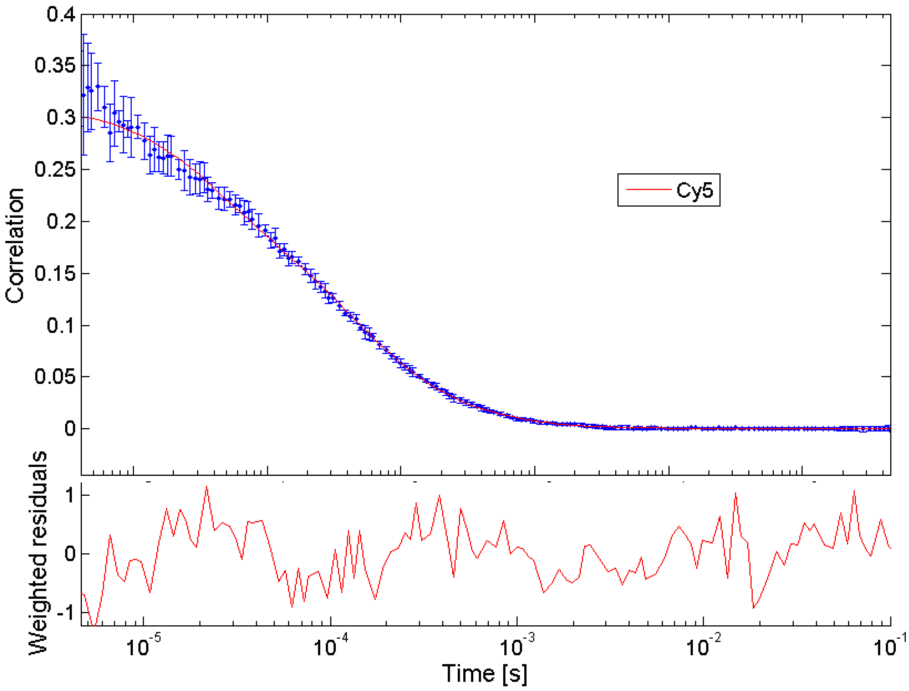

**Figure 24:** Exemplary FCS measurement of Cy5 with weighted fit for determination of red detection volume

From the fits, an averaged structure parameter of $p = 8.1 \pm 0.4$ and an averaged diffusion time of $\tau_D = (0.40 \pm 0.01) ms$ were calculated. This leads to the following red detection volume:

$$\omega_{0R} = 769 \pm 19 nm$$

$$V_R = (7.25 \pm 0.36) \cdot 10^{-15} L.$$

The cross-correlation of a CC60-DNA is displayed in Figure 13. Due to the bigger red probe volume, a higher of number of red labelled molecules is detected, compared to the green volume. This leads to a lower *G(0)* of the red ACF. The height of CCF is at 80% of the lower function, which supports the good alignment of the setup.

The overlap of the red and the green probe volumes is given by using a one-fiber, one-pinhole construct. The only possibility that the probe volumes do not overlap arises from chromatic aberations. A way to make the point-spread-function[3] and therefore the overlap of green and red probe volume visible is to use bead scans.

---

[3] The point spread function (PSF) describes the response of an imaging system to a point source or point object

### 4.1.2.2 Instrument Response Function

For every reasonable lifetime measurement, the instrument response function (IRF) has to be taken into account because every recorded fluorescence decay curve is the convolution of the IRF with the fluorescence response of the molecule. The IRF is the shape of the time spectrum of the excitation pulse and the detector electronics. The IRF can be recorded by reflecting a small portion of the laser pulse into the APD from a sample that does not fluoresce, in our case clean water.

The IRFs of all single-photon APDs have a 'diffusion tail' caused by carrier generation in the neutral layers below the avalanche region. The amplitude of the tail depends on the wavelength and can reach 10 to 20% of the IRF peak (40). Figure 25 shows the response of the setup to the red and the green laser pulse.

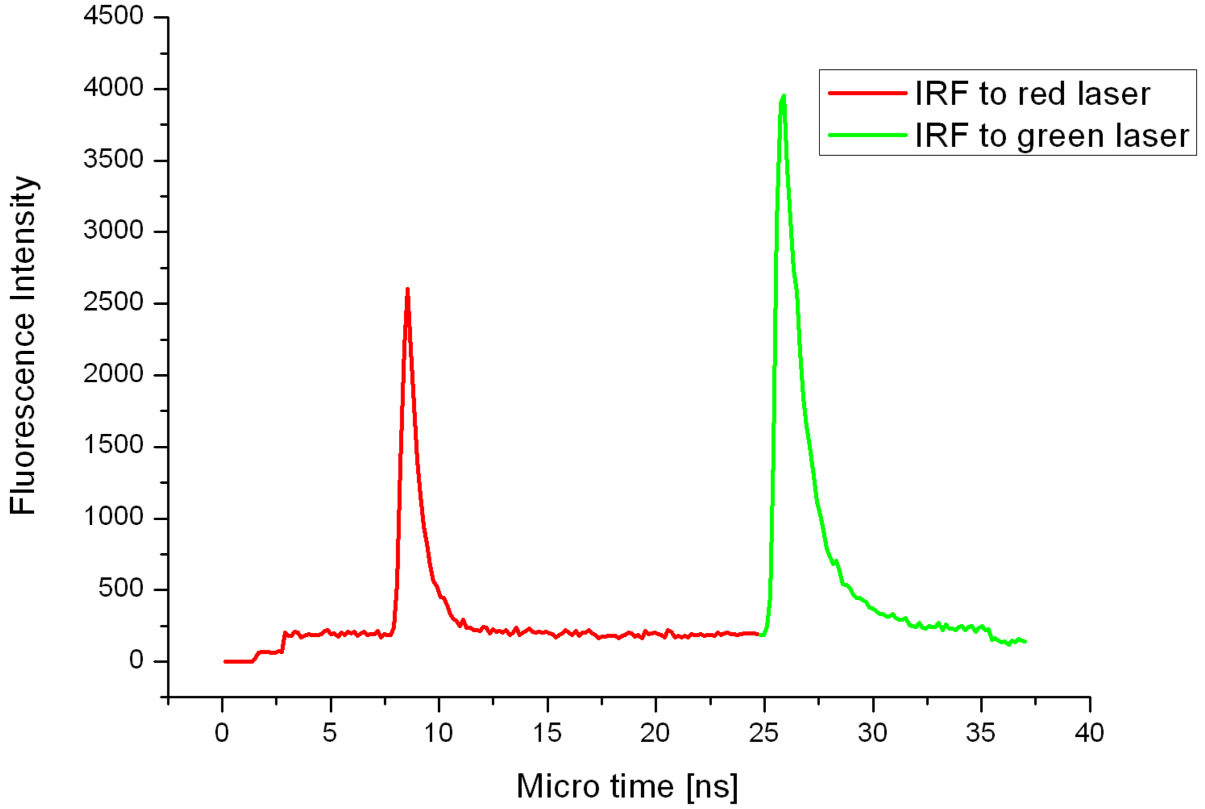

**Figure 25: TCSPC Instrument Response Functions, measured with Becker & Hickl SPC-154. Red: SPCM-AQR-14 for red channels; Green: SPCM-AQR-16 for green channels**

The knowledge of the IRF allows the exact determination of the exact lifetime of the fluorophores measured on this setup. As the IRF depends on the laser settings and the alignment, it needs to be collected for each important measurement series.

### 4.1.2.3 Fundamental Anisotropy Measurements

In order to show the effects of polarization different measurements were taken that show the $\gamma$-factor in both polarizations individually and jointly. As already explained, the $\gamma$-factor is the ratio of red to green detection efficiency. After donor excitation and following fluorescence, the polarization is better maintained than after donor excitation, FRET and subsequent fluorescence. This means that green photons are more likely to maintain the polarization of the laser pulse and therefore the $\gamma$-factor is different for the parallel and the orthagonal detection channels. This is shown in Figure 26:

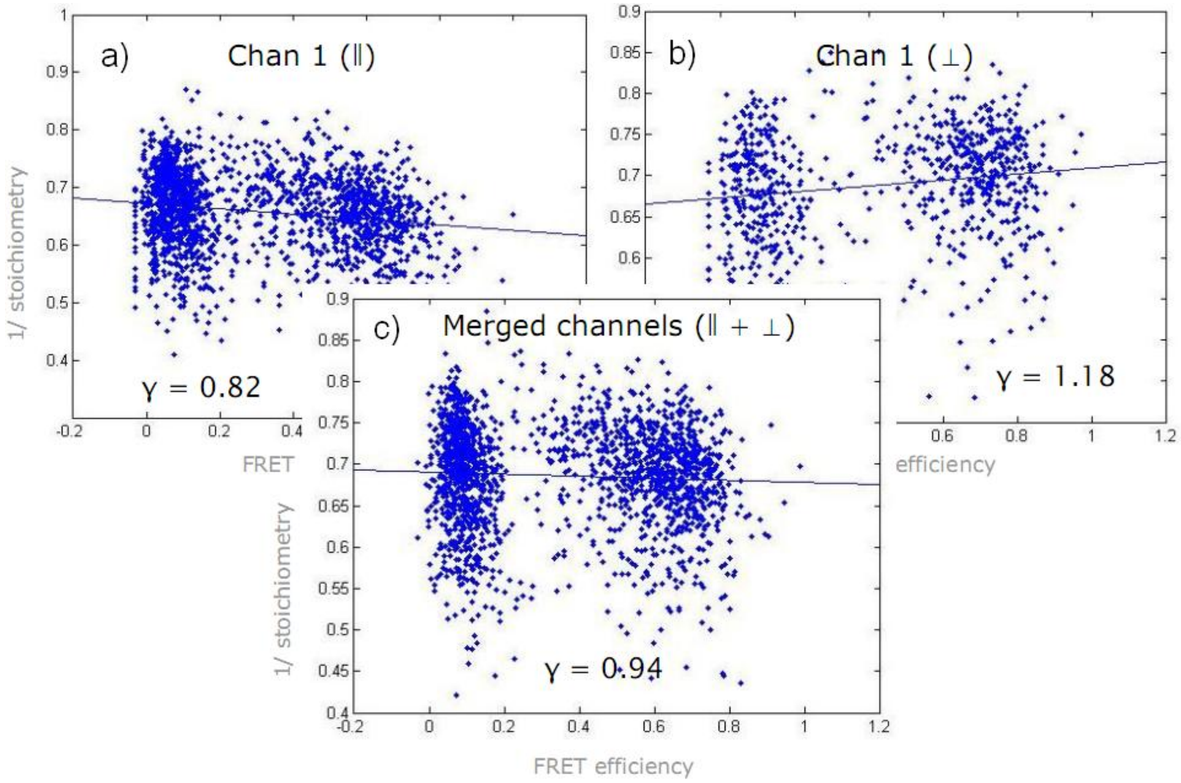

Figure 26: Different ratios of detection efficiencies of green and red molecules

In the next figure, several capabilities of the setup are shown. A high fret DNA was measured for this purpose.

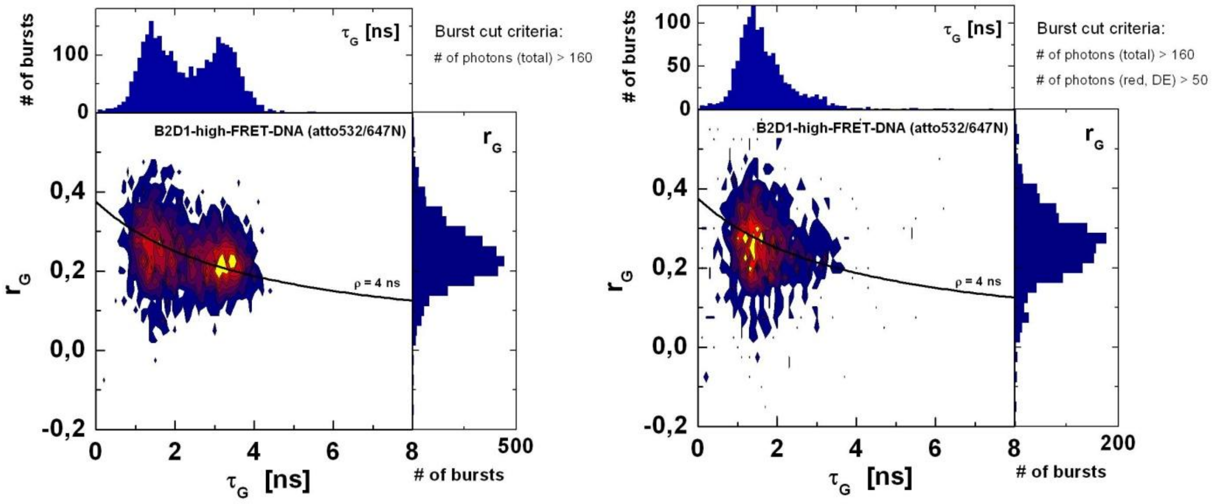

Figure 27: High FRET DNA analyzed without (a) and with PIE (b). The missing population in (b) belongs to donor-only labelled molecules.

For a proper lifetime fit, the data was de-convoluted with the instrument response function and the lifetime $\tau$ is plotted versus the anisotropy.

### 4.1.3 Discussion of the MPF Setup

The central point of the instrument is the confocal volume. As already mentioned, it is in the range of 2 to 7 femptolitres. This is not the minimal volume. The size of the confocal volume is determined by the objective and how much of the back aperture is filled with the laser beam. If the back aperture is completely filled or overfilled, then the size is reduced in lateral and axial direction. For all applications that require the use of FCS a very small volume is required to detect as many events as possible that are influenced by diffusion. On the other hand, for single-molecule measurements, like Burst Analysis, a volume is needed that collects as many photons as possible. A small probe volume, in contrast, offers less background and hence a better contrast. So, an compromise has to be reached. It turns out that the size of our confocal volume is practical for all demands that have been made so far.

Figure 4 displays the emission spectra of the frequently used dyes Atto532 and Atto647N. Ideally, one would like to collect all fluorescent photons the sample emits. This is unfortunately not possible for several reasons. One important criteria is the need to exclude scattered laser light.

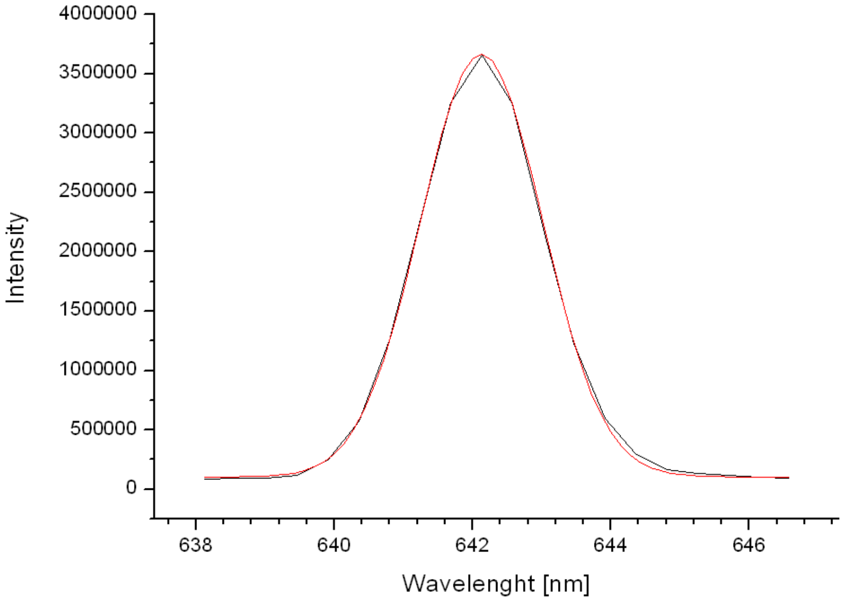

Figure 28: The spectrum of the laser with a peak at 642.1nm and a width of 3.54nm (FWHM)

Figure 35 shows the spectral width of the red laser pulse. Diode lasers don't have a distinct emission but emit over a small spectral range. Hence, the emission filters have to exclude the wavelength of 530 - 534nm and 640 - 645nm. The green fluorescence is collected from 544nm to 640nm, where the dichroic mirror cuts of for the red fluorescence. The spectrum for both emission filters is shown below.

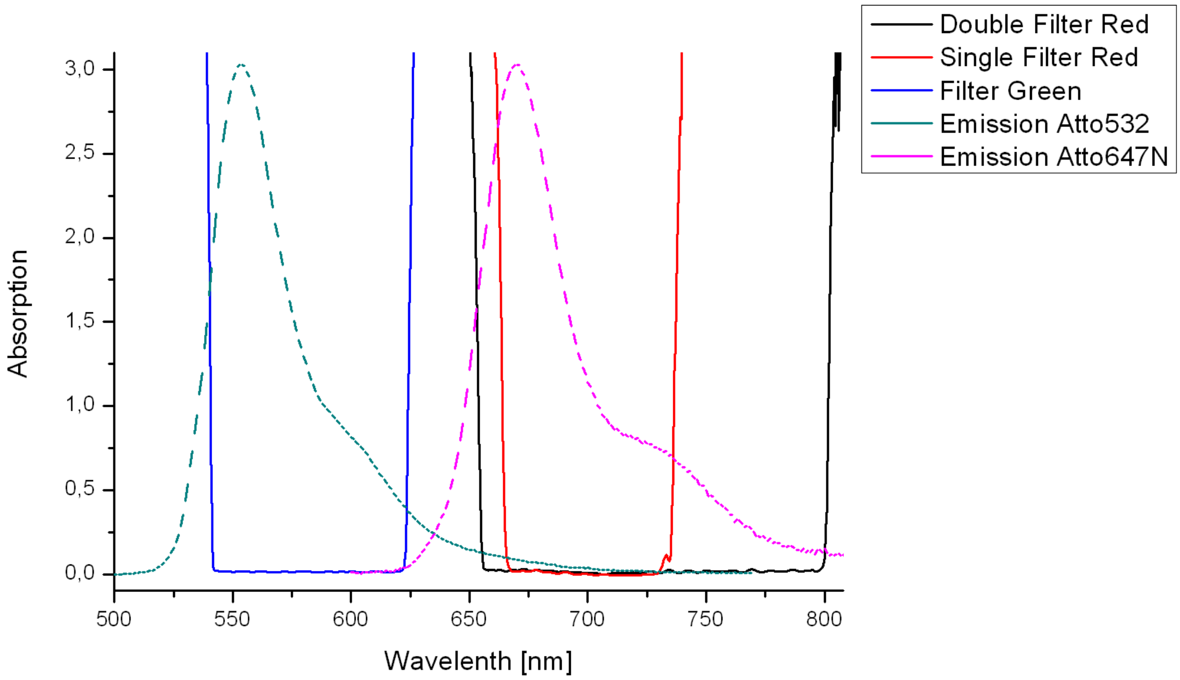

Figure 29: Comparson of filter sets

Initially, a double filter set consisting of a Edge Basic Long Pass Filter (635 LP, AHF analysetechnik, Tübingen, Germany) in combination with a 725/150 Brightline emission filter (HC 725/150, AHF analysetechnik, Tübingen, Germany) was used as an emission filter for the red channel. This decision was made because the double filter is broader and collects more fluorescence photons. By mischance, this double filter set seemed to let through Raman scattering. This resulted in a background signal of 1.5 kHz in the red channels compared to 0.3 kHz in the green channels. By switching to the single, narrower filter, the background was reduced to 0.2 kHz.

After the initial assembly of the setup, FCS curves of labelled Actin were measured (Figure 30). Parallel green fluorescence is depicted in blue and perpendicular green light is shown in red. The amplitudes of the ACFs of the two channels were different, although the photons were coming from the same source. A complete re-adjustment of the setup was unable to remove this artefact. One hint that the alignment was not the problem came from the high amount of dark counts coming from one of the detectors. The according APD was replaced in the course of debugging and measurements repeated, this time with the CC60 DNA.

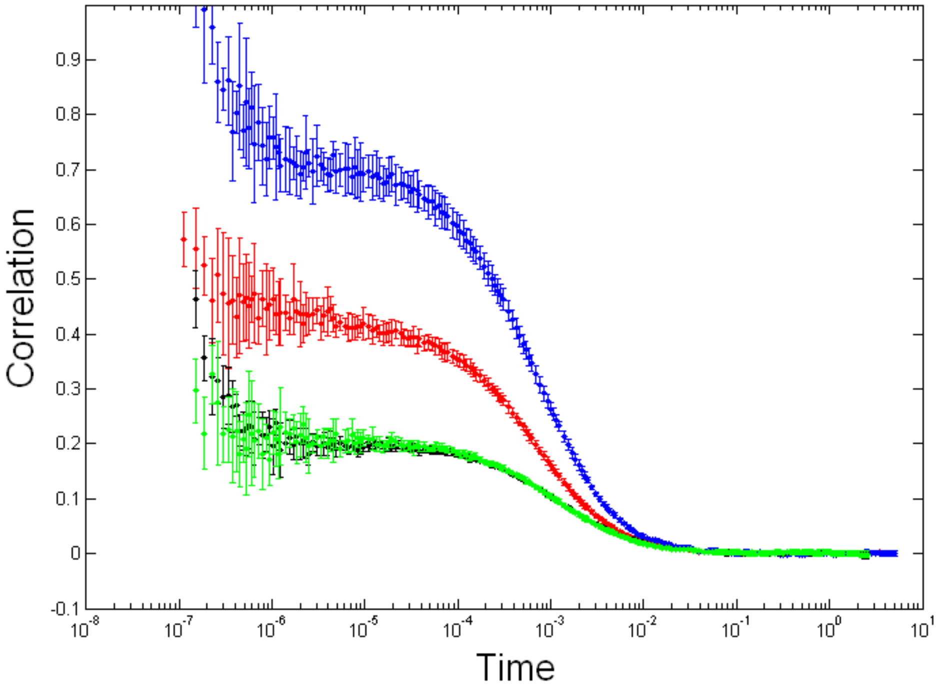

Figure 30: FCS curves of green detectors after first assembly of the setup (red and blue) and after exchange of one APD

As a result, both polarizations showed the expected overlap, shown in the previous Figure with the green and black curve.

After the proper alignment and calibration of the setup, the system is very stable. Only Still, it is recommended that the position of the detectors and the pinhole should be verified every two weeks. Of course, a calibration sample should be measured before any important measurement or series of measurements.

## 4.2 Conformational Changes in Heat Shock Protein 90

### 4.2.1 Biochemical Introduction to Heat Shock Protein 90

Heat shock proteins, as a class, are among the most highly expressed cellular proteins across all species. As their name implies, heat shock proteins protect cells when stressed by elevated temperatures. They account for 1–2% of total protein content in unstressed cells. However, when cells are heated, the fraction of heat shock proteins increases to 4–6% of cellular proteins (41).

The function of the Heat Shock Protein 90 (Hsp90) includes assisting in protein folding, cell signalling, and is responsible for the stabilization and activation of a large number of key regulatory proteins such as the tumor suppressor factor p53. This protein was first isolated by extracting proteins from stressed cells (42). These cells were stressed by heating, dehydrating or by other means, all of which caused the cell's proteins to begin to denature.

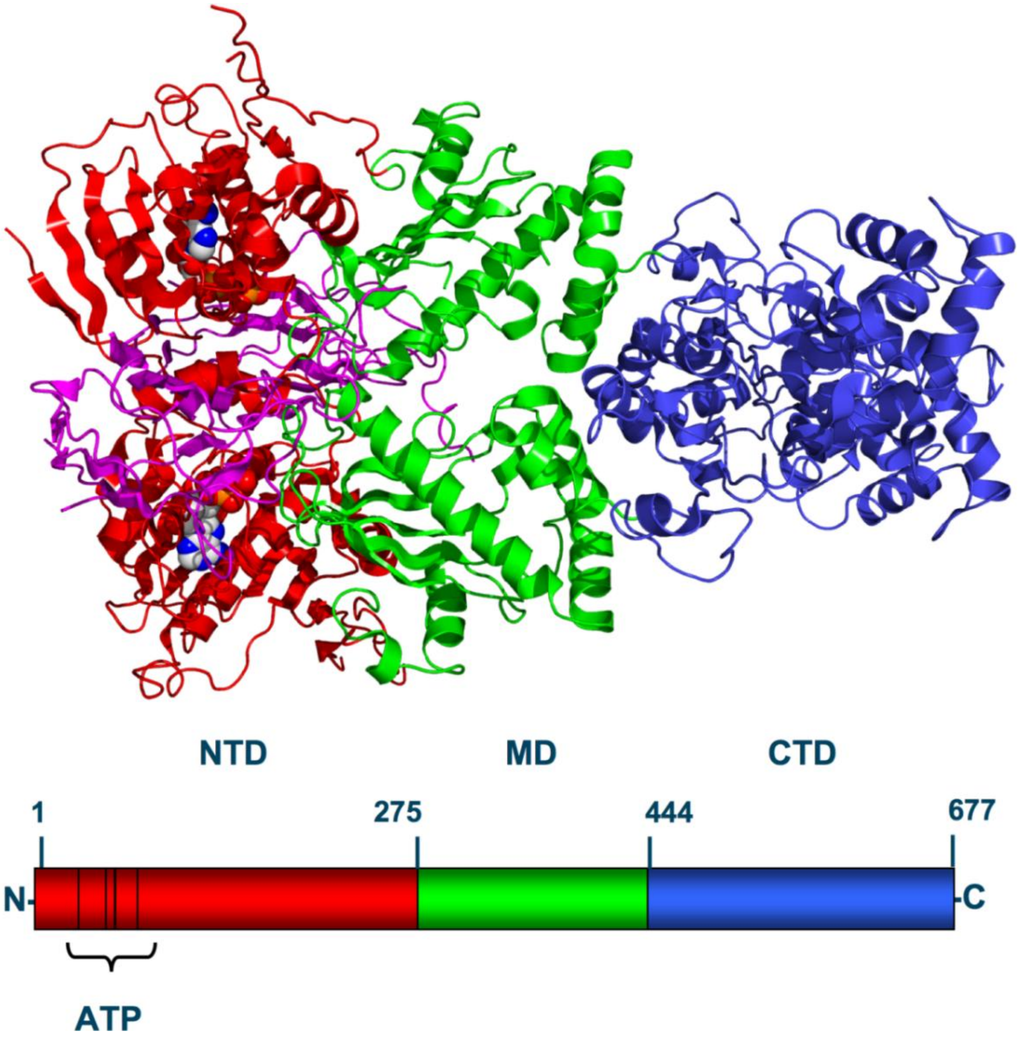

Figure 31: Top: Crystallographic structure of the dimeric Hsp90 in a closed state. Bound ATP molecules are represented by space filling spheres (43). Bottom: 1D sequence of the yeast Hsp90. NTD= N-terminal domain (red), MD = middle domain (green), CTD = C-terminal domain (blue).

The interest on HSP90 has increased significantly over the last few years because it was identified as an important drug target in cancer research. Cancerous cells overexpress a number of proteins, including PI3K and AKT. Inhibition of these two proteins triggers apoptosis. Furthermore, Hsp90 stabilizes the PI3K and AKT proteins. Hence, inhibition of Hsp90 appears to induce apoptosis through inhibition of the PI3K/AKT signalling pathway (44). Another important role of Hsp90 in cancer is the stabilization of mutant proteins, that appear during cell transformation, such as v-Src, the fusion oncogene Bcr/Abl, and p53. It appears that Hsp90 can act as a "protector" of less stable proteins produced by DNA mutations (45). Targeting Hsp90 with drugs has shown promising effects in clinical trials for cancer therapy. For example, the Hsp90 inhibitor geldanamycin has been used as an anti-tumour agent with great success. A 50% reduction in tumour growth has been realized with treatment of geldanamycin. The function of HSP90 is dependent on ATP binding and ATP hydrolysis, but it is currently unclear how ATP affects the suggested conformational changes of Hsp90 (46). Our ambition is now to reveal the conformational changes, that are induced by ATP binding and its hydrolysis.

HSP90 is a homodimer and every unit consists of three domains: N-terminal (NTD), middle (MD) and C-terminal domain (CTD). During the functional cycle of HSP90, the protein opens and closes as shown schematically in Figure 32.

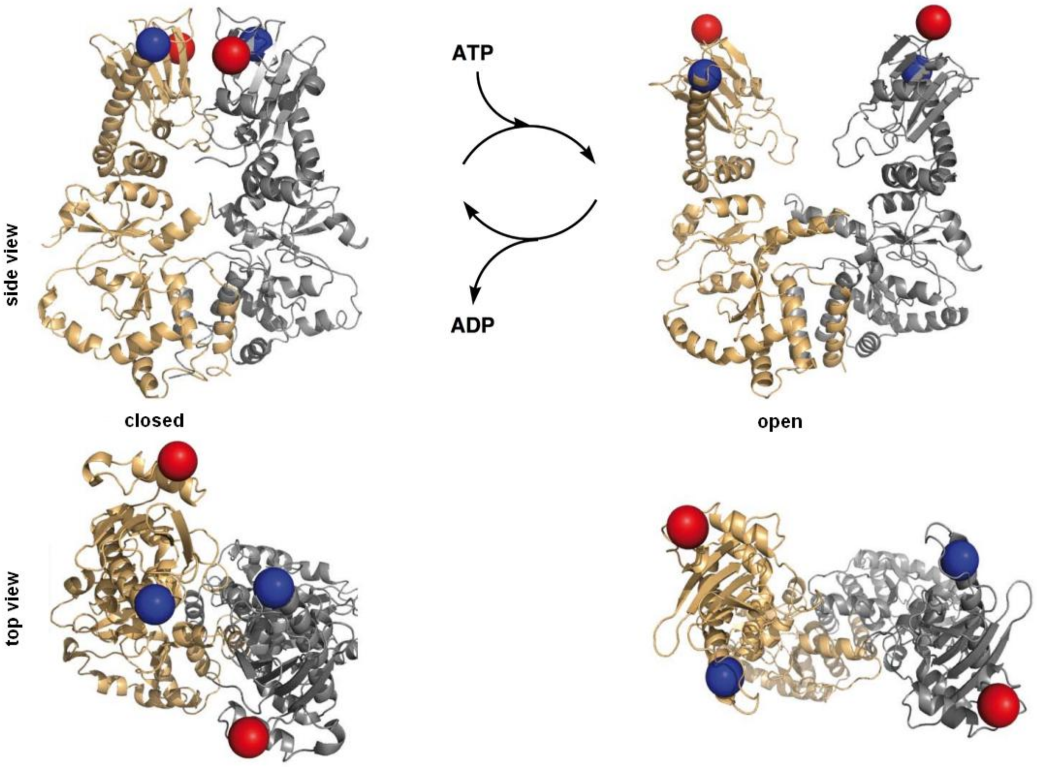

Figure 32: Pincer movement of HSP90 coupled to ATPase activity. ATPase cycle and movement seem to be just weakly coupled. Blue and red spheres stand for donor and acceptor dye, respectively. [Figure adapted from (47)]

It was shown by (48) that the opening and closing of the arms is weakly coupled to the ATPase activity. Additionally, this ATPase reaction is exceptionally slow (less than one hydrolysis per minute) and involves large conformational changes.

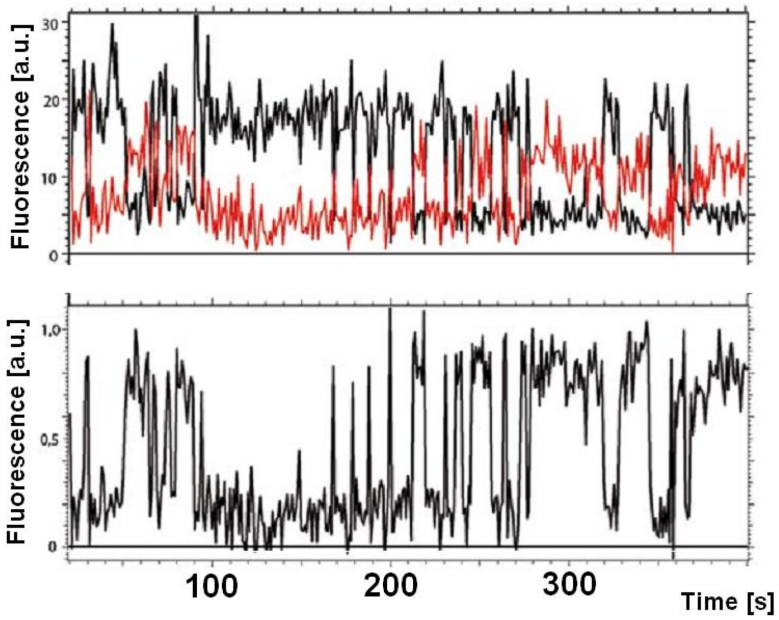

Figure 33: Single molecule FRET time traces recorded in the presence of ATP, recorded on a TIRF-setup (48). Top: Fluorescence signal of the donor (black trace) and the acceptor (red trace). Bottom: Calculated FRET efficiency

Mickler et al. were able to predict four different conformations using Monte Carlo calculations. Several other publications depict cycles with two different closed and two different open structures (49) (50), but only one open and one closed structure has been confirmed by crystal structures.

### 4.2.2 Conformational Changes in HSP 90 Mutants

To investigate the previously discussed open and closed states of HSP90, several mutants have been produced. An overview of all labelling positions is shown in Figure 34. The mutants are labelled with the dyes Atto555 and Atto647N (Atto-Tec, Siegen, Germany).

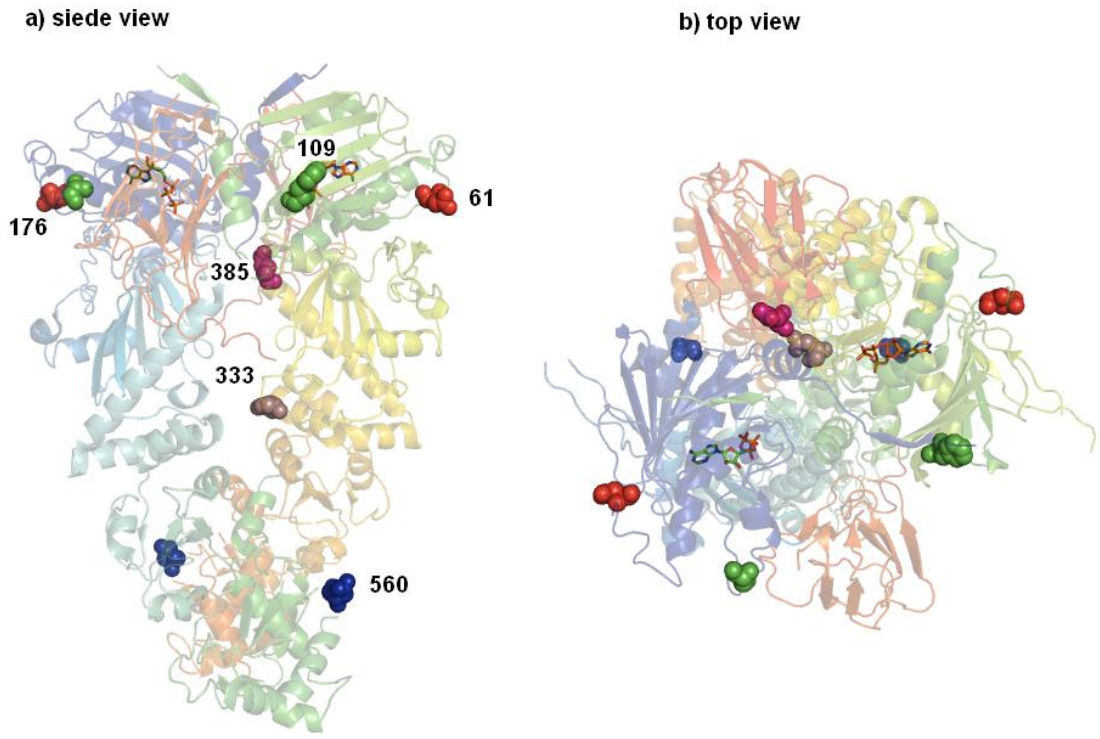

Figure 34: Mutants of HSP90 a) side view of homodimer b) view from top. The position of the cysteine mutants are shown as spaced structures and labelled with the according amino acid number. Delta8 mutant not shown here.

Double labelled mutants were prepared by combining two single mutants. They were mixed together, heated in order to form monomers and cooled again so that heterodimers were formed. These proteins were then purified and measured in the MPF setup. The mutants, that were measured, are labelled with a donor dye at the first position (on one part of the homo-dimer) and with an acceptor at the second position (on the other part of the homo-dimer).The following mutants were produced and measured: 82-560, 109-176, Delta8, 560-560, 61-333, 61-385 and 61-61. The Delta8 mutant misses the last amino acids in order to increase the ATP binding constant.

FCS curves from all measurements were calculated. Figure 35 shows the FCS curve for a mutant (marked on AA 109 and 176). Due to problems with the heating step, no double labelled molecules were detected and FRET efficiencies were not calculated. This happened to the samples 82-560, 109-176 and delta8.

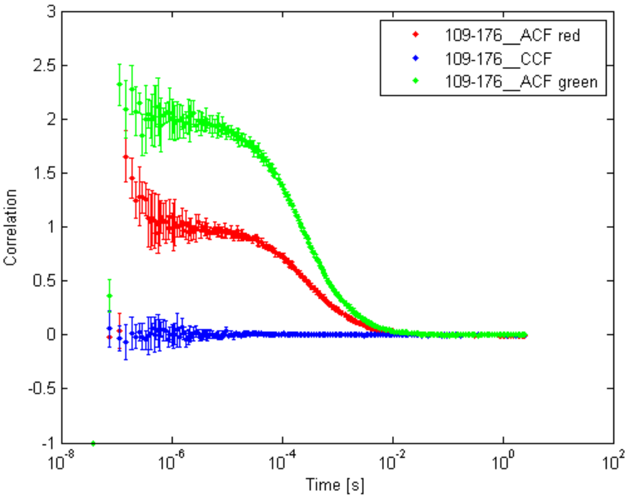

**Figure 35: FCS measurements of the 109-176 mutant with no double-labelled molecules present.**

## 4.2.3 Results of various HSP90 mutants

### *4.2.3.1 560-560 Mutant*

For the mutant that was labelled on both monomeric units at AA 560 experiments were carried out with 2mM AMP-PNP, ATPγS or without nucleotide. The histograms of FRET efficiencies are given in Figure 36. The FRET efficiencies are shifted to lower values in the absence of nucleotide (see chapter 5.6).

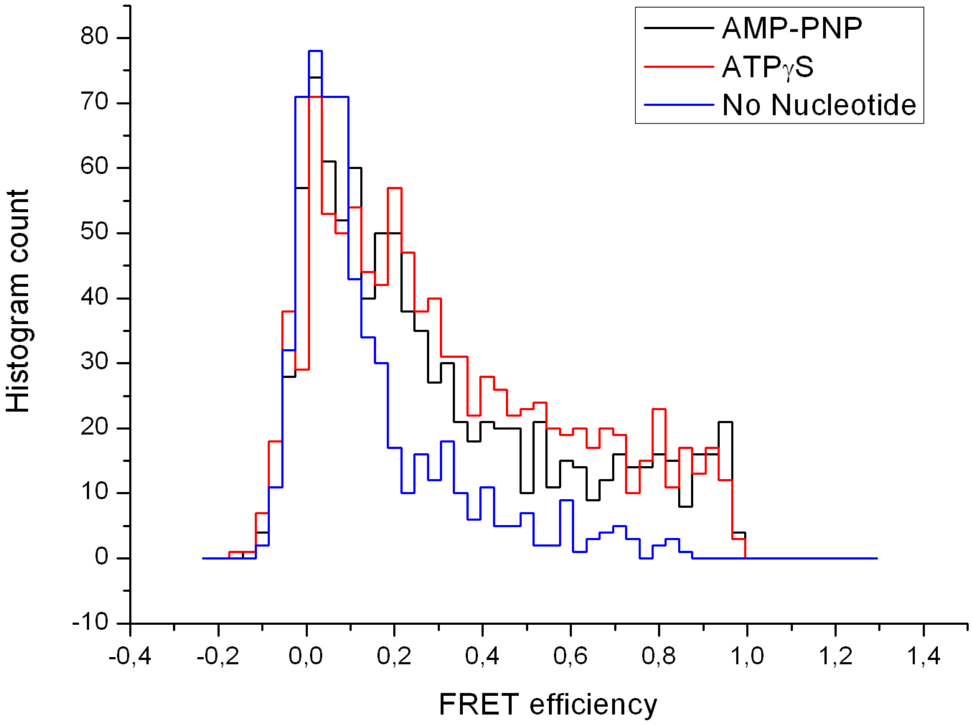

**Figure 36: 560-560 mutant with different nucleotides**

### 4.2.3.2 61-333 Mutant

The 61-333 mutant was measured in the presence of 2mM ATP (Figure 37). The broad distribution with a peak at 30% and a rising peak towards 100% FRET efficiency leads to the assumption that more than one sub-state of this mutant exists. This will be verified in future experiments using PDA.

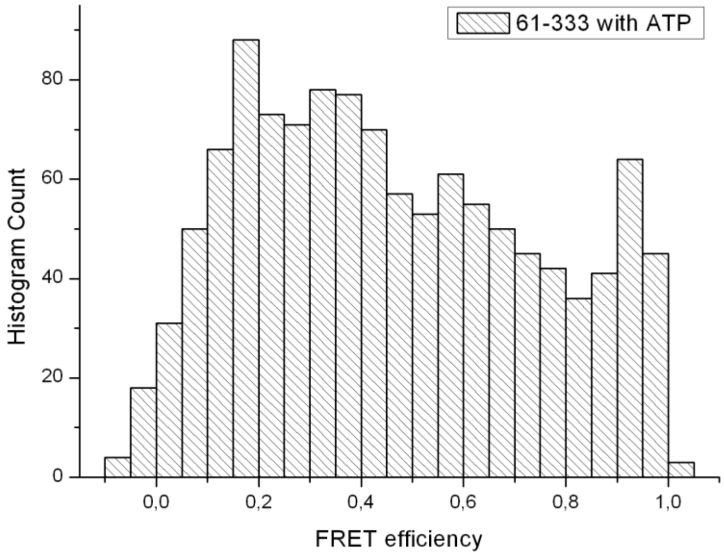

Figure 37: FRET efficiencies of 61-333 Mutant, measured with ATP

### 4.2.3.3 61-385

The 61-385 mutant was measured in the presence of 2mM ATP and the results are shown in Figure 38.

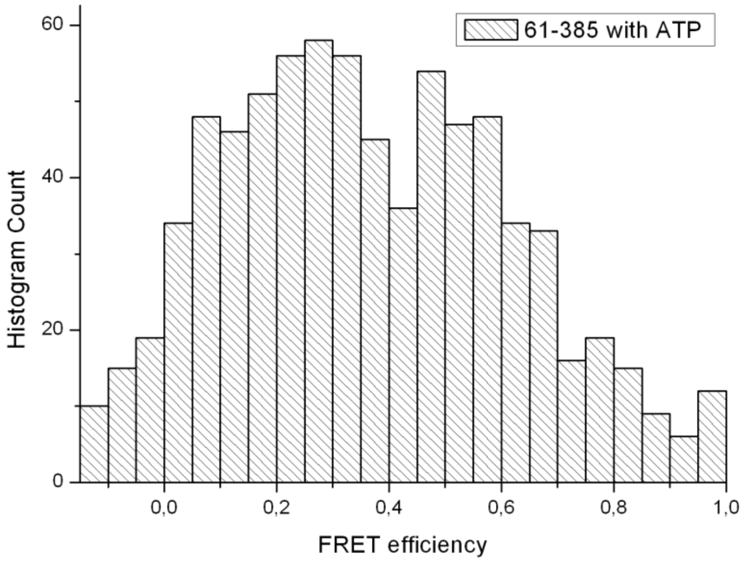

Figure 38: FRET efficiencies of 61-385 with ATP

The local minimum at a FRET efficiency of 40% suggests the presence of at least two sub-populations. Nevertheless, the distributions are broad. This could either be a result of bad photon statistics - which is not the case, because the thresholds were set accordingly. Further analysis with PDA will show if the distribution can be fitted with one or two sub-states.

### 4.2.3.4 61-61 Mutant

The 61-61 mutant was measured in the presence of 2mM ATP (Figure 39).

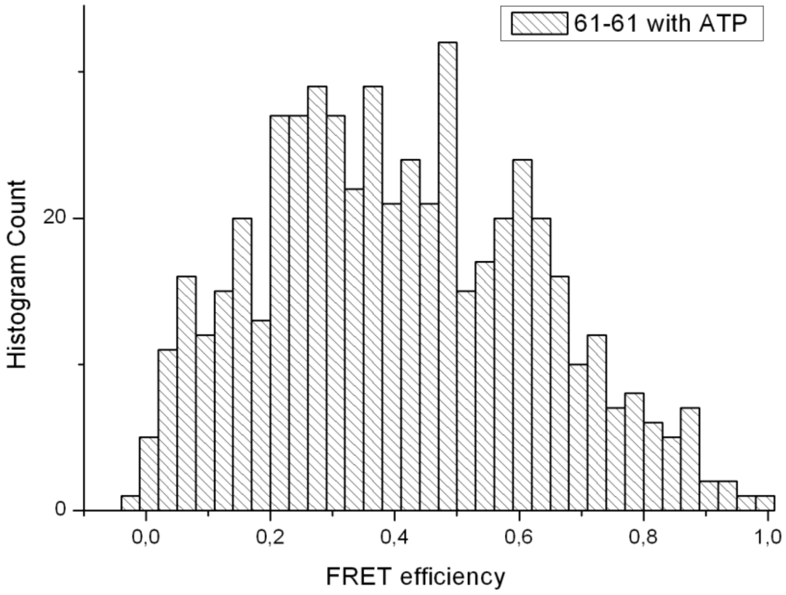

Figure 39: 61-61 mutant measured with ATP

Here again, a very broad distribution of FRET efficiencies is observed. Longer measurement times with this sample would increase the statistics and an analysis using PDA would clarify the number of sub-states.

### 4.2.4 Discussion of HSP90 Data

For several samples, no single-molecule data were obtainable, as shown in Figure 35. The probable cause for this may be difficulties the heating step during the sample preparation. The protein is produced as homodimer, i.e. with donor or acceptor dye attached to the same AA on every monomer. Afterwards, two differently labelled mutants are mixed and heated to 50°C, so that both complexes dissociate into monomers. Under cooling to room temperature a mixture of hetero- and homo-dimers is formed and the two species are separated with HPLC. During this heating step, the protein might be denaturated and form aggregates or the two subunits might not part and samples are either donor or acceptor only.

Most experiments were performed with an additional coiled-coil motif at the C-terminus to prevent dissociation of the dimer. The only exception was the c560 mutant, which lacks this feature. Figure 34 shows that in this case the dyes are attached to the C-terminus. Without nucleotide, the experimental determined $k_D$ is approximately 60nM. The $k_D$ for this mutant with nucleotide is not known so far. The measurement was carried out at a nominal protein concentration of 3nM. This explains very accurately the peak at a FRET efficiency of around zero, because the protein should be in its open state. Addition of nucleotide enhances the affinity between the two monomers and hence, higher FRET efficiencies arise. No clear difference arises from the use of AMP-PNP, that can be hydrolyzed, but much slower than ATP, or the use of ATPγS, that cannot be hydrolyzed at all. All used nucleotides are shown in the figure below.

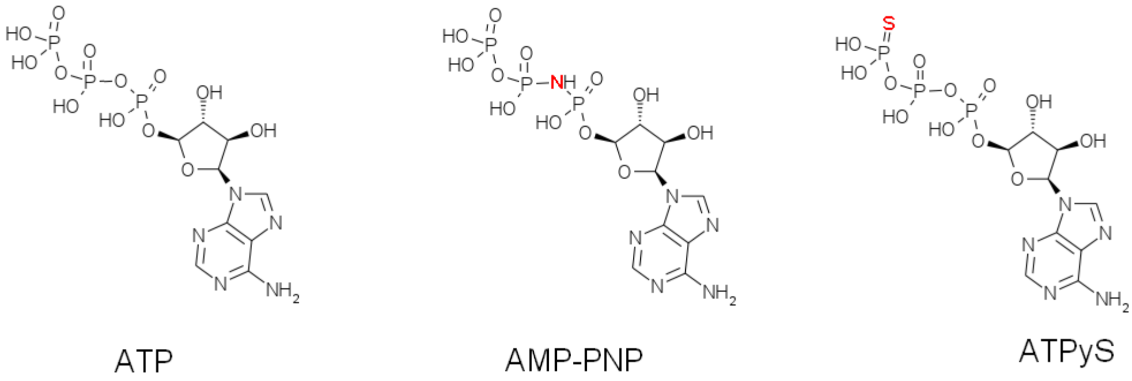
ATP AMP-PNP ATPyS

Figure 40: Three types of Nucleotide used with HSP90

Due to the fact that with PIE only double labelled molecules are taken into account, the remaining peak around zero must be a result of a long-lasting open conformation.

The 61-333 mutant is labelled at the very flexible and dynamic N-terminus. Due to this flexibility this part of the protein was crystallized just recently (51). Our data confirm the common opinion and show a broad distribution of FRET values with two clear maxima at 0.2 and 0.9. Further measurement is needed in order to emphasize the underlying dynamics of this very fast opening and closing of the N-terminus.

The *61-385* and *61-61* mutant show a very similar behaviour. The former exhibits two maxima at 0.3 and 0.5 FRET efficiency. The latter has slightly shifted maxima at 0.3 and 0.6 FRET efficiency. The position of the two dyes on the protein (see Figure 34) suggests that, in the 61-385 mutant, the FRET efficiencies should be shifted to higher values because the distance between the fluorophores is smaller. This is validated by our data. No other comparable single-molecule data of these two mutants have been obtained so far, so it is impossible to implement the measured data into an existing model.

## 4.3 Detailed Insight in the Polymerization of Actin

### 4.3.1 Biochemical Introduction to Actin

Actin is a globular, 42-kDa protein found in all eukaryotic cells (52). Actin was first observed experimentally in 1887 by W.D. Halliburton, who extracted a protein from muscle that 'coagulated' preparations of myosin, and that he dubbed "myosin-ferment" (53). However, Halliburton was unable to further characterise his findings, and the discovery of actin is attributed to Brúnó F. Straub (54). The crystal structure of monomeric actin (G-actin) was solved in 1990 *Kabsch et al* (55). In the same year, a model for filamentous or polymeric (F-actin) was proposed by *Holmes et al* (56).

Actin is the monomeric subunit of microfilaments, one of the three major components of the cytoskeleton. The other two components are vimentin or keratin, which belong to the class of intermediate filaments. The third class are microtubules, like the mitotic spindle.

Actin belongs also to the group of thin filaments, which are part of the contractile apparatus in muscle cells. Figure 41 shows the crystal structure of G- and F-actin.

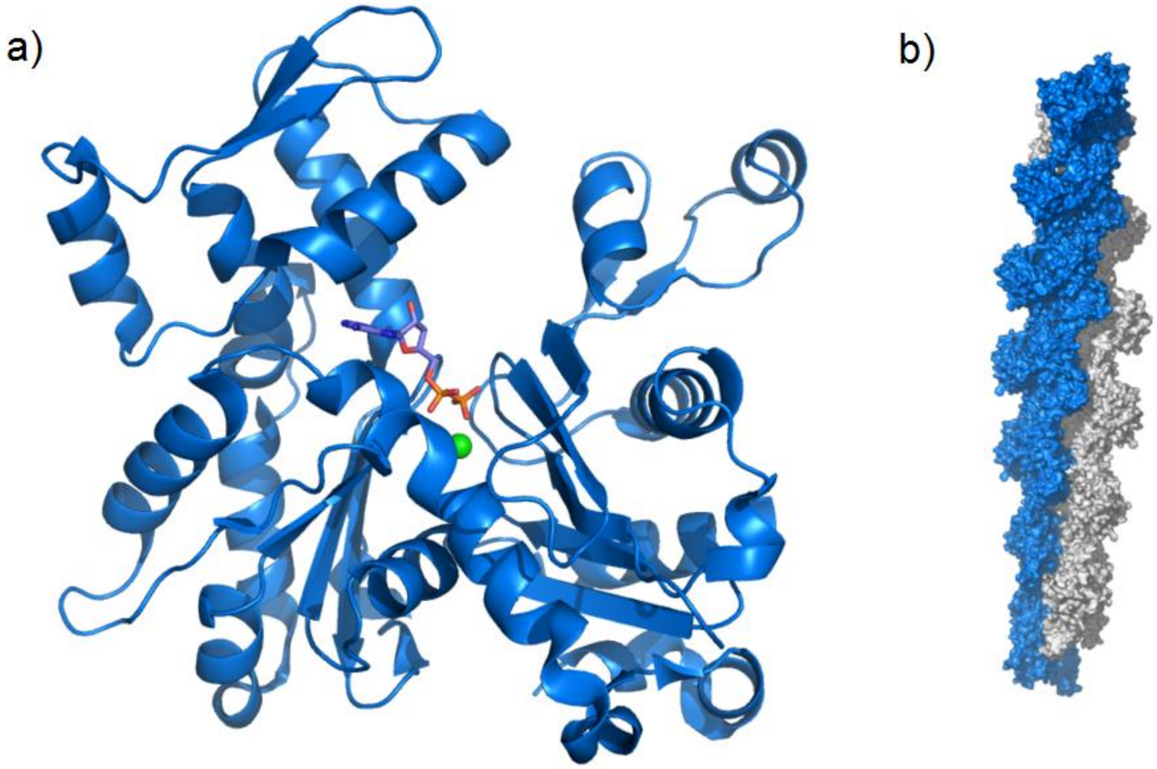

Figure 41: a) Crystal structure of monomeric actin with bound ATP b) Filamental actin [structures taken from www.rcsb.org]

Actin has different functions in the cell: besides the already mentioned function as stabilizer for the cell in the cytoskeleton. In addition, it hardwires the cytoplasm with the surroundings to support signal transduction. It also allows cell motility, which is the ability to move spontaneously and actively. In muscle cells, it acts as the scaffold on which myosin proteins generate force to support muscle contraction. In non-muscle cells, it serves as a track for cargo transport myosins such as myosin V and VI.

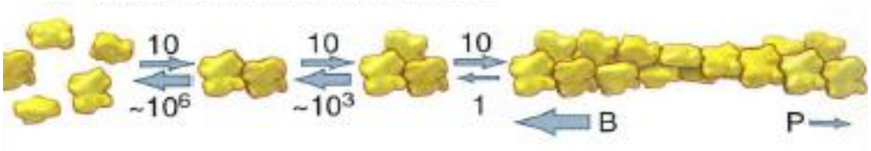

Figure 42: Unfavourable start of actin nucleation (57)

Figure 42 shows the formation of dimers and trimers, which is very unfavourable due to the rapid dissociation of the subunits. According to this kinetic model, tetramers are the first really stable oligomers and result in instantaneous polymerization. Thus, the start of the polymerization has not yet been observed. Also, the critical concentration of actin – the concentration where polymerization starts – is unknown.

Oda et al. recently found a new, flat conformation of actin by preparing well-ordered actin filaments in a 18 tesla magnet field (58). This transition of G- to F-actin is accompanied by a relative rotation of two major domains, shown in Figure 43. They also proved that this flat conformation is associated with the polymerization and the release of phosphate.

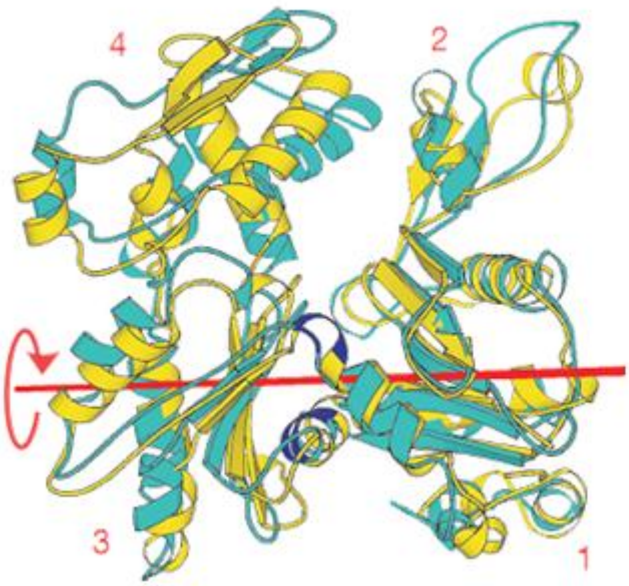

Figure 43: Transition between the G- and F-Structure of actin subunits

The correlation between release of phosphate and polymerization should make it possible to lower the critical concentration. A lower critical concentration would increase the amount of dimers and trimers formed at a concentration where analysis methods like FCS or PCH are aplicably.

### 4.3.2 Results of the Polymerization of Actin

Our goal in investigating the actin polymerization is to gain insight into the initial steps of the polymerization process. Due to the very small relative concentrations of dimers and trimers, it was never possible to detect them in solution. In addition, the exact critical concentration for polymerization has not yet been determined. Some preliminary measurements show that it is possible with our MPF setup to follow the polymerization in detail over at least 48 hours. Initial experiments were performed, using the new six-hole sample holder, filled with actin in concentrations of 50 nM, 100 nM and 150 nM. The actin monomers are labelled with TAMRA (Invitrogen, Carlsbad, USA) with a labelling efficiency of 95%. Each concentration was measured twice, once in G-buffer, a buffer that is low on $Mg^{2+}$-ions and hence represses the polymerization and once in F-buffer, which allows polymerization. Using G-buffer, we could demonstrate that the samples are stable over days and no artefacts due to drying, laser radiation or evaporation were observed.

In F-Buffer, polymer formation was already seen at 100 nM (Figure 44). As the number of actin monomers in the filament increases, the brightness of the filament increases. In addition, the average number of monomers within the probe volume decreases. The next step is to quantify the monomer concentration in solution as a function of time.

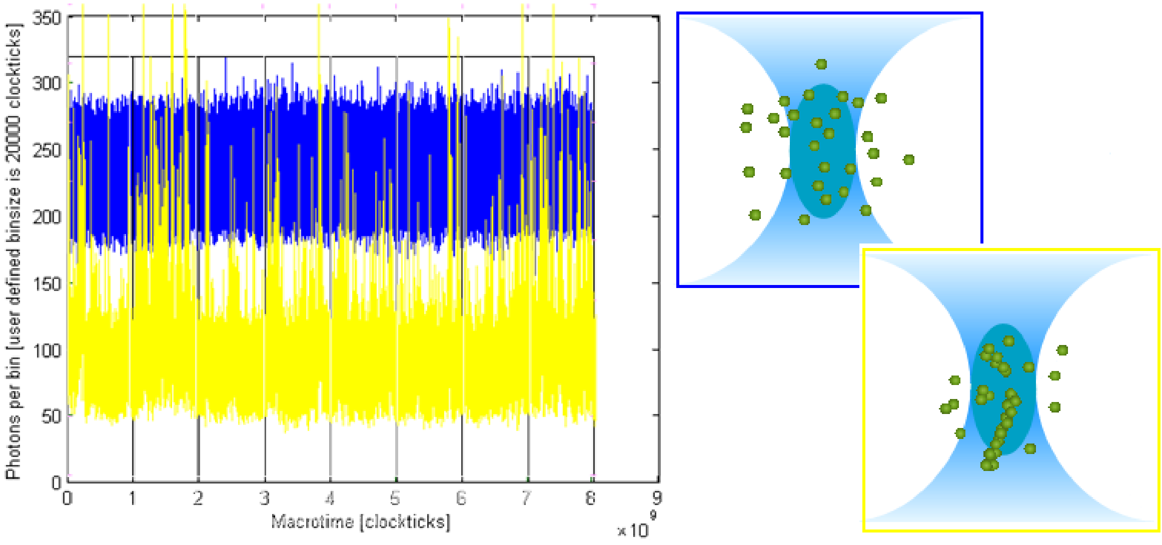

Figure 44: 100 nM actin sample at t=0 (blue) and t=48 h (yellow)

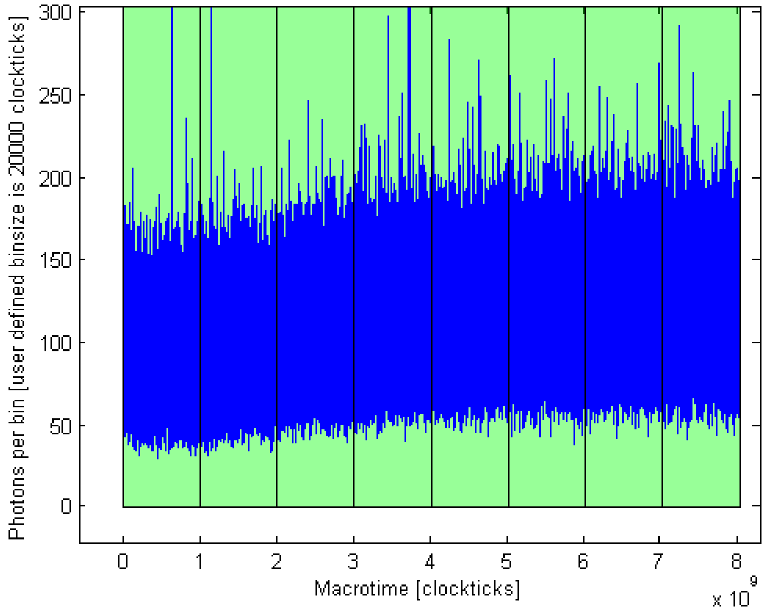

Figure 45: Increase of fluorescence after change from G- to F-buffer

Figure 45 shows the first measurement directly after transferring the actin from G-buffer, where it is stored, to f-buffer. A clear increase of fluorescence intensity is observable. This change arises from a change of the chemical environment of the fluorophore, as discussed in chapter 5.8.

### 4.3.3 Discussion of the Polymerization of Actin

In order to investigate the increase of fluorescence at the beginning of the measurement, actin in G-Buffer was placed in a fluorescence spectrometer and the fluorescence spectrum was collected. The ion concentration was increased to the level of F-buffer and the spectrum was measured again.

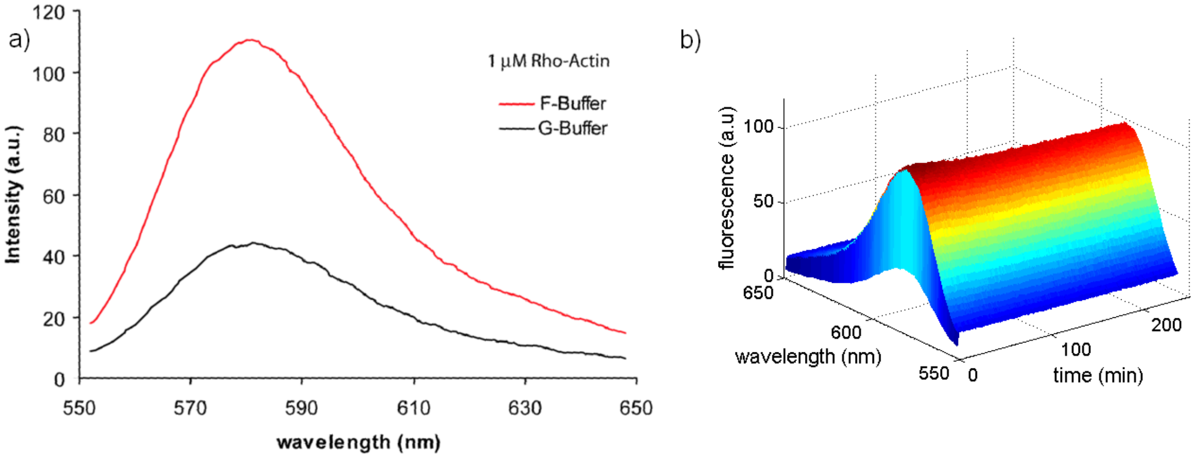

Figure 46: a) Increase of Fluorescence Intensity due to buffer change b) small fluorescence intensity decrease due to bleaching

Figure 46 a) shows the nearly threefold increase in fluorescence due to buffer. The following decrease can arise from either bleaching of fluorophores or from quenching that occurs during polymerization. Figure 46 b) proofs that the fluorescence in F-buffer stays stable after initial photobleaching.

Several challenges arise when using the multi-sample holder. For example, it is not possible to use water as the immersion medium, as it evaporates within the first hour. Instead, a special immersion oil, *Immersol W* (Zeiss, Feldbach, Switzerland) was used. This oil has the same index of refraction as water.

The polymerization can be measured through the development of spikes in the time trace. Another approach quantifying polymerization is measuring the decrease of the basis count rate that is directly depending on the average concentration of monomers in solution, shown in Figure 44. Due to time limitations, it was not possible to obtain the full concentration dependence of the polymerization.

# Chapter 5: Summary and Outlook

## 5.1 MPF-Setup

The primary objective of this work was to build a confocal Multi-Parameter Fluorescence Setup, which extracts the maximum amount of information out of every photon, and investigate biological systems, using this system. The successfully construct of the MPF setup, its characterization and application has been discussed.

Anisotropy measurements, fluorescence correlation spectroscopy and single molecule FRET measurements were performed. The green and the red volumes have sizes of 2.12 and 7.25 femptolitres, respectively. The overlap of both volumes is given by the special design of the setup, but this has to be verified using bead scans. The motorized stage mounted on the microscope is not sufficient for this purpose. Thus, a nano-positioning piezostage has to installed on the setup. With the piezo stage, it would also be possible to collect confocal images in living cells with MPF information.

Improvements have been made regarding the ability to perform long-term measurements. A sample holder was constructed and the software was written in order to follow reactions under different conditions over at least 48 hours.

For better shielding of the setup, an opaque box has to be constructed and installed about the detection path.

## 5.2 Heat Shock Protein 90

Several mutants of HSP90 were measured in single-molecule experiments in order to figure out the dynamics of this protein and its ATP dependency. Here, we could proof the common belief, that the N-terminus of the protein is very flexible, but exhibits two slightly favoured positions. All mutants feature a coiled coil motif to prevent parting of the two subunits, except the *c560*-mutant. So one could argue that that the peak of FRET efficiencies around zero arises from donor-only monomers, but PIE eliminates all donor- and acceptor-only molecules. This suggets that the C-terminus is open most of the time and just closes in the presence of a nucleotide.

Up to now, the experiments with HSP90 were limited to timescales in the order of milli-seconds, the diffusion time of the molecules through the confocal spot. However, there might be slow dynamics overlaying the very fast opening and closing of the different termini. So one possibility would be to enclose the protein into vesicles in order to increase the hydrodynamic radius and slow down the diffusion process. Another approach could be the immobilization of HSP90 in a TIRF setup that is also capable of PIE (59).

In order to determine whether HSP90 dynamically fluctuates between sub-states, a hidden Markov Model could be applied (60). This would not only lead to the fact that the number of states could be determined objectively, but also has the advantage that the real distances between the dyes could be calculated more precisely. These distances can then be used to test the hypothesis of four different conformations, predicted by *Mickler et al* (48).

## 5.3 Actin

Preliminary results with the MPF setup showed that it is possible to follow the polymerization of actin over 48 hours. The next step in this approach is to correlate the decrease of the monomer signal to the decrease in monomer concentration. In addition, the length of the polymers can be calculated from its brightness. The dependency of the TAMRA dye on its chemical environment was shown as well.

In order to obtain a rate constant for actin dimerization, the following approach could be pursued: Two actin monomers that are labelled with different dyes are connected with a linker (Figure 47).

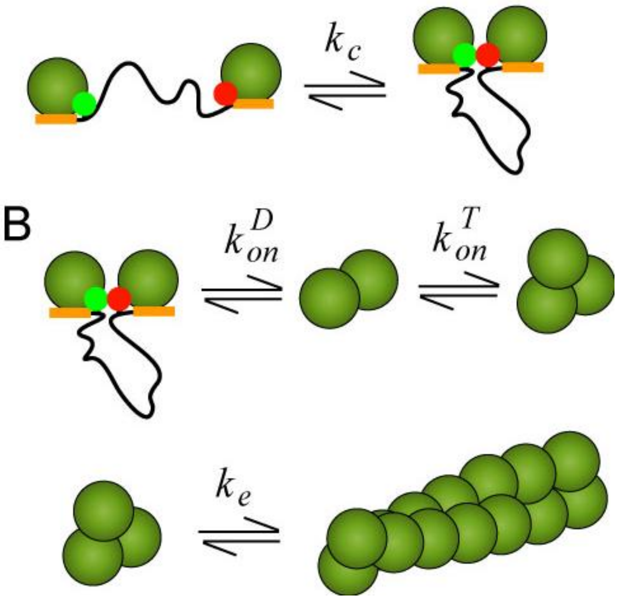

Figure 47: Linking of two actin monomers for rate constant of dimerization

Measuring FRET efficiencies of this modified actin allows an estimation of how much time the molecule dwells in the monomeric or dimeric state.

A different approach would be to determine the exact molecular brightness of monomers and linked dimers. In solutions that are slightly under the critical concentration, it could be possible to observe trimerisation and, from their concentration, estimate the rate constant for trimer formation.

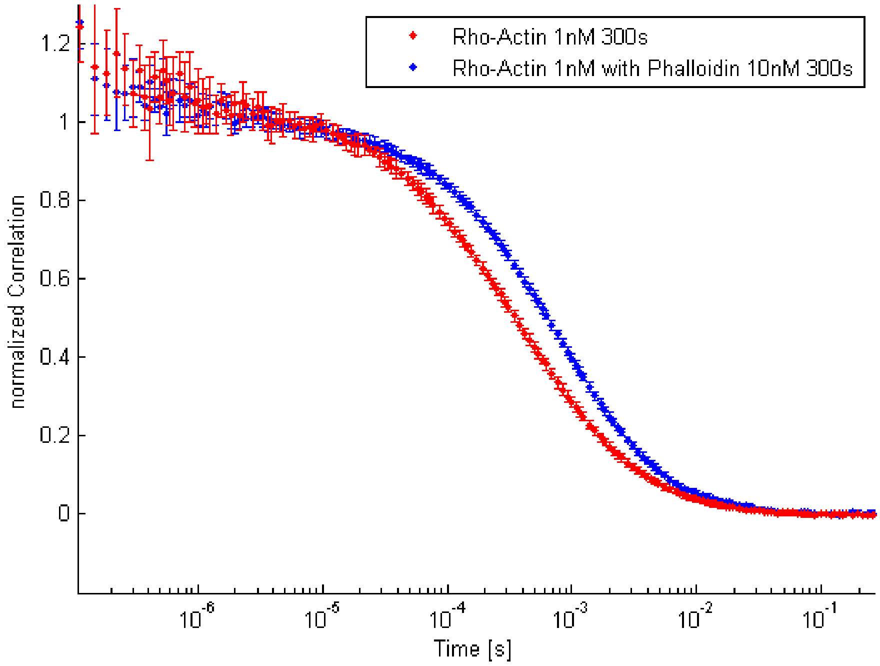

Figure 48: Normalized ACF of labelled actin with or without phalloidin

In this context, the influence of Phalloidin has to be investigated. Phalloidin decreases the critical concentration by stabilizing either dimers or trimers. The exact species, which is stabilized, is not yet known. Figure 48 shows the increase of diffusion time in a 1 nM solution of Actin in G-buffer whan phalloidin is present.

# Abbreviations

| | |
|---|---|
| ACF | Autocorrelation function |
| APD | Avalanche photodiode |
| CCF | Crosscorrelation function |
| FCS | Fluorescence correlation spectroscopy |
| FRET | Förster/Fluorescence resonance energy transfer |
| HSP | Heat shock protein |
| IRF | Instrument response function |
| MPF | Multi-parameter fluorescence |
| PBS | Polarizing beam splitter cube |
| PIE | Pulsed interleaved excitation |
| TCSPC | time correlated single photon counting |
| TTTR | Time Tagged, Time Related |
| WDM | Wavelength division multiplexer |

# References

1. Rotman, B. 1961. Measurement of activity of single molecules of beta-D-galactosidase. Proc Natl Acad Sci U S A 47:1981-1991.
2. Ashkin, A. 1970. Acceleration and Trapping of Particles by Radiation Pressure. Phys. Rev. Lett. 24.
3. Gosse, C., and V. Croquette. 2002. Magnetic tweezers: micromanipulation and force measurement at the molecular level. Biophys J 82:3314-3329.
4. Binnig, G., C. F. Quate, and C. Gerber. 1986. Atomic Force Microscope. Physical Review Letters 56:930.
5. Schmidt, T., G. J. Schutz, W. Baumgartner, H. J. Gruber, and H. Schindler. 1996. Imaging of single molecule diffusion. Proc Natl Acad Sci U S A 93:2926-2929.
6. Axelrod, D., T. P. Burghardt, and N. L. Thompson. 1984. Total internal reflection fluorescence. Annu Rev Biophys Bioeng 13:247-268.
7. Minsky, M. 1961. Microscopy Apparatus. USA.
8. Hirschfeld, T. 1976. Quantum efficiency independence of the time integrated emission from a fluorescent molecule. Applied Optics 15.
9. Moerner, W. E., and D. P. Fromm. 2003. Methods of single-molecule fluorescence spectroscopy and microscopy. Review of Scientific Instruments 74:3597-3619.
10. Anazawa, T., Matsunaga H., Yeung E.S. 2002. Electrophoretic quantitation of nucleic acids without amplification by single-molecule imaging. Analytical Chemistry 74.
11. Förster, T. 1948. Zwischenmolekulare Energiewanderung und Fluoreszenz. Annalen der Physik 2.
12. Stryer, L., and R. P. Haugland. 1967. Energy transfer: a spectroscopic ruler. Proc Natl Acad Sci U S A 58:719-726.
13. Yildiz, A., J. N. Forkey, S. A. McKinney, T. Ha, Y. E. Goldman, and P. R. Selvin. 2003. Myosin V walks hand-over-hand: single fluorophore imaging with 1.5-nm localization. Science 300:2061-2065.
14. Bismuto E., M. E. D., Pleus S., Sikor M., Röcker C., Nienhaus G.U. and Lamb D.C. 2009. Molecular Dynamics Simulation of Acidic Compact State of Apomyglobin from Yellowfin Tuna. PROTEINS: Structure, Function, and Bioinformatics accepted.
15. Stone, M. D., M. Mihalusova, M. O'Connor C, R. Prathapam, K. Collins, and X. Zhuang. 2007. Stepwise protein-mediated RNA folding directs assembly of telomerase ribonucleoprotein. Nature 446:458-461.
16. Schwille, P. Fluorescence Correlation Spectroscopy.
17. Dertinger, T., V. Pacheco, I. von der Hocht, R. Hartmann, I. Gregor, and J. Enderlein. 2007. Two-focus fluorescence correlation spectroscopy: a new tool for accurate and absolute diffusion measurements. Chemphyschem 8:433-443.
18. Schwille, P., U. Haupts, S. Maiti, and W. W. Webb. 1999. Molecular dynamics in living cells observed by fluorescence correlation spectroscopy with one- and two-photon excitation. Biophys J 77:2251-2265.
19. Patel, R. C., U. Kumar, D. C. Lamb, J. S. Eid, M. Rocheville, M. Grant, A. Rani, T. Hazlett, S. C. Patel, E. Gratton, and Y. C. Patel. 2002. Ligand binding to somatostatin receptors induces receptor-specific oligomer formation in live cells. Proc Natl Acad Sci U S A 99:3294-3299.
20. Muller, B. K., E. Zaychikov, C. Brauchle, and D. C. Lamb. 2005. Pulsed interleaved excitation. Biophys J 89:3508-3522.
21. Wouters, F. S., P. J. Verveer, and P. I. Bastiaens. 2001. Imaging biochemistry inside cells. Trends Cell Biol 11:203-211.

22. Oida, T., Y. Sako, and A. Kusumi. 1993. Fluorescence lifetime imaging microscopy (flimscopy). Methodology development and application to studies of endosome fusion in single cells. Biophys J 64:676-685.
23. Clegg, R. M. 1996. Fluorescence Resonance Energy Transfer, Fluorescence Imaging. John Wiley & Sons, New York.
24. Müller, B. K. 2006. Die gepulste alternierende Anregung in der konfokalen Fluoreszenzspektroskopie: Entwicklung und Anwendungen. In Fakultät für Chemie und Pharmazie. Ludwig-Maximilians-Universität München, München.
25. Shinitzky, M., and Y. Barenholz. 1978. Fluidity parameters of lipid regions determined by fluorescence polarization. Biochim Biophys Acta 515:367-394.
26. Hohng, S., C. Joo, and T. Ha. 2004. Single-molecule three-color FRET. Biophys J 87:1328-1337.
27. Chen, Y., J. D. Muller, P. T. So, and E. Gratton. 1999. The photon counting histogram in fluorescence fluctuation spectroscopy. Biophys J 77:553-567.
28. Magde, D., E. Elson, and W. W. Webb. 1972. Thermodynamic Fluctuations in a Reacting System&#151;Measurement by Fluorescence Correlation Spectroscopy. Physical Review Letters 29:705.
29. Elson E. L., M. D. 1974. Fluorescence correlation spectroscopy. I. Conceptual basis and theory. Biopolymers 13:1-27.
30. Douglas Magde, E. L. E. W. W. W. 1974. Fluorescence correlation spectroscopy. II. An experimental realization. Biopolymers 13:29-61.
31. Einstein, A. 1905. Über die von der molekularkinetischen Theorie der Wärme geforderte Bewegung von in ruhenden Flüssigkeiten suspendierten Teilchen. Annalen der Physik 17.
32. Smoluchowski, M. 1906. Zur kinetischen Theorie der brownschen Molekularbewegung und der Suspensionen. Annalen der Physik 21:756.
33. Stokes, G. G. 1880. Mathematical and physical papers. Reprinted from the original journals and transactions, with additional notes by the author. Cambridge University Press, Cambridge.
34. Schwille, P., F. J. Meyer-Almes, and R. Rigler. 1997. Dual-color fluorescence cross-correlation spectroscopy for multicomponent diffusional analysis in solution. Biophys J 72:1878-1886.
35. Eggeling, C., C. Ringemann, R. Medda, G. Schwarzmann, K. Sandhoff, S. Polyakova, V. N. Belov, B. Hein, C. von Middendorff, A. Schonle, and S. W. Hell. 2009. Direct observation of the nanoscale dynamics of membrane lipids in a living cell. Nature 457:1159-1162.
36. Deniz, A. A., M. Dahan, J. R. Grunwell, T. Ha, A. E. Faulhaber, D. S. Chemla, S. Weiss, and P. G. Schultz. 1999. Single-pair fluorescence resonance energy transfer on freely diffusing molecules: observation of Forster distance dependence and subpopulations. Proc Natl Acad Sci U S A 96:3670-3675.
37. Sabanayagam C.R., E. J. S., Meller A. 2005. Using fluorescence resonance energy transfer to measure distances along individual DNA molecules: Corrections due to nonideal transfer. Journal of Chemical Physics 6.
38. Kapanidis, A. N., N. K. Lee, T. A. Laurence, S. Doose, E. Margeat, and S. Weiss. 2004. Fluorescence-aided molecule sorting: analysis of structure and interactions by alternating-laser excitation of single molecules. Proc Natl Acad Sci U S A 101:8936-8941.
39. Muller, C. B., A. Loman, V. Pacheco, F. Koberling, D. Willbold, W. Richtering, and J. Enderlein. 2008. Precise measurement of diffusion by multi-color dual-focus fluorescence correlation spectroscopy. EPL (Europhysics Letters) 83:46001.
40. Becker, W. 2009. The bh TCSPC Handbook.
41. Gilles Crevel, H. B., Hella Huikeshoven, and Sue Cotterill. The Drosophila Dpit47 protein is a nuclear Hsp90 co-chaperone that interacts with DNA polymerase J. Cell Sci. 114.
42. Wegele, H., L. Muller, and J. Buchner. 2004. Hsp70 and Hsp90--a relay team for protein folding. Rev Physiol Biochem Pharmacol 151:1-44.
43. Ali, M. M., S. M. Roe, C. K. Vaughan, P. Meyer, B. Panaretou, P. W. Piper, C. Prodromou, and L. H. Pearl. 2006. Crystal structure of an Hsp90-nucleotide-p23/Sba1 closed chaperone complex. Nature 440:1013-1017.

44. Stebbins, C. E., A. A. Russo, C. Schneider, N. Rosen, F. U. Hartl, and N. P. Pavletich. 1997. Crystal structure of an Hsp90-geldanamycin complex: targeting of a protein chaperone by an antitumor agent. Cell 89:239-250.
45. Calderwood, S. K., M. A. Khaleque, D. B. Sawyer, and D. R. Ciocca. 2006. Heat shock proteins in cancer: chaperones of tumorigenesis. Trends Biochem Sci 31:164-172.
46. Richter, K., and J. Buchner. 2006. hsp90: twist and fold. Cell 127:251-253.
47. Mickler, M. 2008. Der ATPase-Zyklus von Hsp90 in Einzelmolekül-FRET-Experimenten. In Fakultät at für Physik. Technische Universität, München.
48. Mickler, M., M. Hessling, C. Ratzke, J. Buchner, and T. Hugel. 2009. The large conformational changes of Hsp90 are only weakly coupled to ATP hydrolysis. Nat Struct Mol Biol 16:281-286.
49. Weikl, T., P. Muschler, K. Richter, T. Veit, J. Reinstein, and J. Buchner. 2000. C-terminal regions of Hsp90 are important for trapping the nucleotide during the ATPase cycle. J Mol Biol 303:583-592.
50. Bron, P., E. Giudice, J. P. Rolland, R. M. Buey, P. Barbier, J. F. Diaz, V. Peyrot, D. Thomas, and C. Garnier. 2008. Apo-Hsp90 coexists in two open conformational states in solution. Biol Cell 100:413-425.
51. Pearl, L. H., and C. Prodromou. 2006. Structure and mechanism of the Hsp90 molecular chaperone machinery. Annu Rev Biochem 75:271-294.
52. Stryer, L. 2003. Biochemie. Spektrum Akademischer Verlag, Heidelberg.
53. Halliburton, W. D. 1887. On Muscle-Plasma. J Physiol 8:133-202.
54. Straub, F. B., and G. Feuer. 1989. Adenosinetriphosphate. The functional group of actin. 1950. Biochim Biophys Acta 1000:180-195.
55. Kabsch, W., H. G. Mannherz, D. Suck, E. F. Pai, and K. C. Holmes. 1990. Atomic structure of the actin:DNase I complex. Nature 347:37-44.
56. Holmes, K. C., D. Popp, W. Gebhard, and W. Kabsch. 1990. Atomic model of the actin filament. Nature 347:44-49.
57. Earnshaw, P. a. 2007. Cell Biology. Spektrum Akademischer Verlag, Heidelberg.
58. Oda, T., M. Iwasa, T. Aihara, Y. Maeda, and A. Narita. 2009. The nature of the globular- to fibrous-actin transition. Nature 457:441-445.
59. Kapanidis, A. N., T. A. Laurence, N. K. Lee, E. Margeat, X. Kong, and S. Weiss. 2005. Alternating-laser excitation of single molecules. Acc Chem Res 38:523-533.
60. McKinney, S. A., C. Joo, and T. Ha. 2006. Analysis of single-molecule FRET trajectories using hidden Markov modeling. Biophys J 91:1941-1951.